ELECTROSTATIC PROTON CYCLOTRON HARMONIC WAVES OBSERVED WITH THE ALOUETTE II SATELLITE

by

ROBERT WALTER HARVEY

B.Sc., The University of British Columbia, 1966

A THESIS SUBMITTED IN PARTIAL FULFILMENT OF

THE REQUIREMENTS FOR THE DEGREE OF

MASTER OF SCIENCE

in the Department

of

GEOPHYSICS

We accept this thesis as conforming to the

required standard

THE UNIVERSITY OF BRITISH COLUMBIA

April, 1969

In presenting this thesis in partial fulfilment of the requirements for an advanced degree at the University of British Columbia, I agree that the Library shall make it freely available for reference and Study. I further agree that permission for extensive copying of this thesis for scholarly purposes may be granted by the Head of my Department or by his representatives. It is understood that copying or publication of this thesis for financial gain shall not be allowed without my written permission.

Department of Geophysics

The University of British Columbia
Vancouver 8, Canada

Date 14th May, 1969.

ABSTRACT

An ELF noise band observed by the Alouette II satellite has been studied. A digital power spectrum program was set up in order to investigate in detail the noise band spectra. Primary results from this analysis are that: a) for altitudes 500-3000 Km. and all geomagnetic latitudes, sharp lower cutoffs of the noise band occur within ~30Hz of the calculated gyrofrequency, b) upper cutoffs to the noise band occur frequently near harmonics of the gyrofrequency, and c) the noise appears to be Doppler shifted when the angle between the velocity vector of the satellite and the geomagnetic field is near 90°.

The occurrence pattern of the noise band has been investigated using available Rayspan analyzed data for epoch 1966. This analysis indicated a pronounced daytime maximum of occurrence.

It is shown that almost all aspects of the noise band may be interpreted in terms of the hypothesis of ambient electrostatic proton cyclotron harmonic waves in the ionosphere, and the concomitant accessibility conditions in the spatially varying geomagnetic field.

TABLE OF CONTENTS

LIST OF FIGURES

LIST OF TABLES

ACKNOWLEDGEMENTS

I express my appreciation and gratitude to my thesis advisor Dr. Tomiya Watanbe who interested me in the Alouette II satellite experiment, encouraged me to look for warm plasma effects in the data, and then discussed the data and theory in this thesis with myself.

I thank Dr. J.A. Jacobs and Dr. R.D. Russell for encouragement in this work.

I gratefully acknowledge the many helpful discussions and suggestions of Dr. R.E. Barrington, of the Defence Research Telecommunications Establishment, Ottawa. I thank also Mr. W.E. Mather for much assistance in the analog data analysis, Mr. R.W. Herring for a 'fast Fourier transform' algorithm, Mr. Scott Inrig for provision of the analog/digital control program, and other members of the DRTE for comments and suggestions.

CHAPTER 1

INTRODUCTION

Very low frequency (VLF) broad-band receivers have been flown in a number of ionospheric satellites. Spectrum analysis of the observed signals has shown the existence of a variety of quasi-continuous bands of noise, and also discrete emissions with rapidly varying frequency-time characteristics (Taylor and Gurnett, 1968). Included in these observations are the more well known phenomena of 'whistlers', 'polar chorus', and the low hybrid resonance (LHR) noise band. These signals are due to the existence of electromagnetic and electrostatic waves propagating in the ionospheric plasma.

In this thesis, data from the Alouette II satellite will be used. This space-craft was built by the Defence Research Telecommunications Establishment (D.R.T.E.), Ottawa, and launched by the National Aeronautics and Space Administration of the U.S.A. on November 29, 1965. Nominal parameters of its orbit are shown in Table I.

The chief interest will be a band of noise which occurs in ~50% of the Alouette II VLF records, and for which the following spectral characteristics are established: 1) a sharp lower frequency cutoff (i.e., intensity decrease) which occurs very near to the proton gyrofrequency, 2) an upper frequency cutoff which is often quite sharp and near harmonics of the gyrofrequency, and 3) occasionally, an apparent harmonic structure.

TABLE I
ORBITAL PARAMETERS OF ALOUETTE II (Jan 12, 1966)

Apogee	2981.82 Km.
Perigee	502.16 Km.
Inclination	78.828 prograde.
Period	121.369 min. - .00006 min/day.
Argument of Perigee	248.25° - 1.8922°/day.
R.A. of Ascending node	172.422° - .7922°/day.
Eccentricity	0.15268.

Examples of this noise band can be seen in Figures 4 and 5. Similar noise has been noted by Guthart et al., (1968) from OGO2 satellite data, and by Burns (1966) and Gurnett and Burns (1968) from Injun III data.

In geophysics two different approaches can generally be taken for the analysis of a series of observations --- particular events, which clearly exhibit the phenomena of interest, may be singled out and analyzed in detail --- or, the gross statistical properties of the observations may be obtained with a view to relating these to other known processes. In this thesis, both approaches are taken. Analysis of existing spectra, obtained by use of analog equipment, has been carried out for a large sample of satellite passes, and the statistics or occurrence pattern of the noise band and certain of its easily identifiable spectral characteristics, computed. However, analog spectrum analysis was not considered sufficient to explore in detail the spectral characteristics of the noise band. A digital spectrum analysis system was set up for this purpose. This is a new application of digital 'fast fourier transform' techniques, and is proving to be quite fruitful for VLF data interpretation. In particular, high resolution determinations of the lower frequency cutoff of the noise band were obtained. Typical results are shown in Figures 7 to 11.

Guthart et al (1968) have considered possible explanations for a noise band which has a lower frequency cutoff near the gyrofrequency, and concluded that electrostatic proton cyclotron harmonic waves (hereafter, proton CH waves; also termed in the literature 'Berstein' modes, Berstein (1958)) were involved. According to Stix (1962), three wave modes can propagate at such frequencies --- left- and right-hand polarized electromagnetic (EM) waves and electrostatic proton CH waves.

However, immediately above the proton gyrofrequency only the right-hand EM and proton CH waves propagate. Considering the right-hand mode, waves propagating parallel to the ambient magnetic field are unaffected by the gyrofrequency. But recent studies by Fredricks (1968) indicate some gyrofrequency effect on perpendicularly propagating EM waves; the magnitude of this effect under ionospheric conditions is not known. Further discussion on this is included in Chapter 7. On the other hand, proton CH waves in a Maxwellian plasma of electrons and protons propagate unattenuated in the direction perpendicular to the ambient magnetic field, and exist above but not immediately below the proton gyrofrequency. Thus following Guthart et al., a band of noise in the ionosphere due to these waves could be expected to have a sharp cutoff in amplitude at the proton gyrofrequency. This explanation of the noise band will be extended.

The presentation of this thesis will be as follows. As a background on the results, details of the Alouette II receiver and antennas, and then methods of spectrum analysis --- both analog and digital --- are examined. Particular spectral characteristics of the noise band, and then its general occurrence pattern are next presented. With a view to explaining these observations on the noise band, a chapter will be devoted to a review of relevant features of proton CH waves. It is then shown that in addition to the sharp lower cutoff all other specific spectral characteristics and some of the general occurrence patterns of the noise band may be explained consistent with the hypothesis of ambient proton CH waves in the ionosphere. Other possible explanations for the noise band are also examined.

CHAPTER 2

THE ALOUETTE II VLF EXPERIMENT

2.1 Receiver System

Alouette II is equipped with a set of capacitively blocked dipole antennas with tip to tip length of 240 feet. The output of these antennas is amplified by an untuned receiver of bandwidth 50 Hz - 30 KHz. Gain of the receiver is controlled by an automatic gain control (AGC) circuit. Both receiver output and AGC voltage are telemetered to the ground.

The receiver-AGC system has been calibrated in the laboratory by applying a signal to the inputs and monitoring the receiver output and AGC voltages (Henderson and Cote, 1967). Typical results at 1 KHz were that a 12 dB increase in receiver input caused a 1 dB increase in receiver output, and a 1 volt increase in the AGC voltages. This holds true quite well over a dynamic range of ~ 60 dB. So, as the receiver input increases, gain of the system is decreased.

2.2 Sheath Effects and Antenna Gain

Gain of the antenna is not so easily estimated as for the VLF receiver. Effects of the ionospheric plasma on dipoles are not well understood. However, a few of the factors which must be considered in determinations of antenna gain will be reviewed.

The antennas and satellite body are electrically floating in the ionospheric plasma, and will come to equilibrium with no net current flowing to them. Due to the high mobility of electrons relative to the heavier ions, they assume a negative potential (the floating potential) different from the potential of the local plasma (the plasma potential). This gives rise to a region surrounding the antennas and satellite body of primarily

positive ions, and a few electrons (the ion "sheath"). Effects of the sheath on measurements of differences in plasma potential (due to electromagnetic and electrostatic waves) are capacitive and resistive. The antennas of Alouette II, which are capacitively blocked, and insulated from the satellite body by 1 meter long non-conducting sleeves, may be represented to a first approximation as in the following figure.

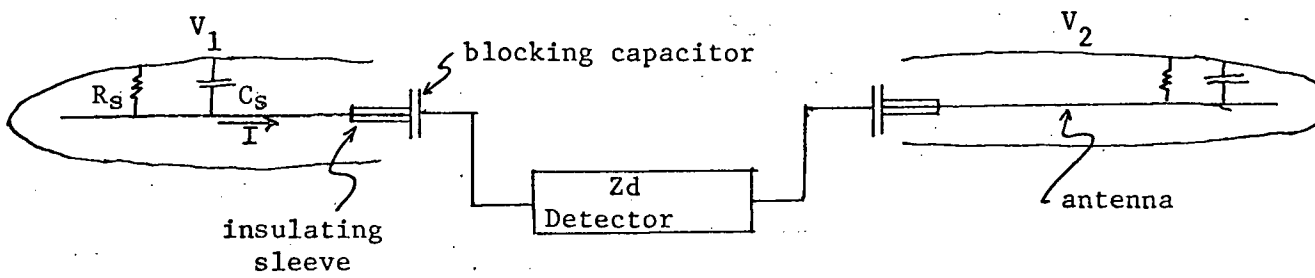

Figure 1
Model for an electric dipole antenna in a plasma

where

Rs, Cs = the resistance and capacitance of the sheath.
V_1, V_2 = different plasma potentials.
Zd = the detector impedance.
I = current.

Then

$$V_1 - V_2 = I(Zs + Zd)$$
$$Zs = \left(\frac{1}{R_s} + j\omega C_s\right)^{-1}$$

Thus the effect of the sheath impedance is to degrade the observed voltage across the detector. A more complete discussion of this model is given by Storey (1963). Simplified considerations indicate, over an effective length of 120 ft. and at frequency 1 KHz, that the magnitude of the sheath impedance for each antenna element is 50 KΩ - j 100 KΩ. However, since the antennas used for the VLF experiment are also used by the

"topside-sounder" experiment, low VLF receiver input impedance had to be chosen in order to insure compatibility; impedance of the receiver through the coupling network is estimated to be quite variable at the low frequency end of the VLF band, being 1 KΩ at 100 Hz to 7 KΩ at 1 KHz. Absolute electric field measurements are thus not feasible because of the uncertainty in the impedance of both the sheath and the receiver.

There are also orientation effects on the sheath when the satellite is in a magnetized plasma. Storey has argued that since the plasma conducts best in the direction of the magnetic field, then the effective area of contact of the antenna with the ambient plasma is the sheath area projected in the magnetic field direction; this area is minimum when the antennas are aligned with the magnetic field. Thus antenna gain will be greatest when the antennas are perpendicular to the ambient magnetic field and least when they are parallel to it.

Another effect leading to orientation-sensitive gain of the antenna is the induced potential due to motion of the spacecraft across magnetic field lines. For the Alouette II, this induced potential ($\vec{V} \times \vec{B}.d\vec{\ell}$) may amount to as much as 10 volts over each half of the antennas. Effects of this potential have been considered by Dickinson (1964). He finds that when $\vec{V} \times \vec{B}.d\vec{\ell}$ is maximum (that is, $d\vec{\ell}$ the antenna orientation vector is perpendicular to $\vec{V} \times \vec{B}$) that the sheath on each antenna element may be distorted to a "tear-drop" shape, one end with zero sheath radius and thus at plasma potential, and the other end with a maximum sheath radius. This maximum sheath radius is ~2cm. at low latitudes and ~90cm. at high latitudes. Thus induced voltage can strongly perturb the sheath and lead to a direct coupling of an electric field in the plasma to one end of each antenna element. The gain of the antennas would be expected to be

increased due to this effect.

Thus there are at least two phenomena which lead to minimum gain of the antennas when they are aligned parallel to the ambient magnetic field. The possible significance of this will be pointed out in a later section in connection with "spin modulation".

CHAPTER 3

SPECTRUM ANALYSIS

The Alouette II VLF receiver signal is stored in an analog mode on precision magnetic tapes. Interpretation of these signals is usually facilitated by spectrum analysis. Figures 4 and 6 illustrate two methods commonly seen in the literature for displaying VLF data. These figures represent the result of analog methods of spectrum analysis. In addition to this type of analysis, a system was set up employing 'fast Fourier transforms' of the digitized VLF signal; this technique gave detailed spectra of the noise band, as shown in Figures 7 to 11. In order to compare the advantages and disadvantages of the above analyses, the equipment and methods to produce these spectra will be discussed.

3.1 Analog Spectrum Analysis

3.1.1 The Rayspan Spectrum Analyzer

The Rayspan consists of a band of 420 band-pass (magnetostrictive) filters spaced with center frequencies on the average 25 Hz apart. These filters are fed in parallel by the VLF signal. Outputs of the filters are sampled by a high speed capacitive commutator, and the results after passing through a logrithmic amplifier are displayed by intensity modulation of synchronized sweeps on a CRT. 35 mm. film is rolled past the CRT screen at a uniform rate. Thus a frequency versus time display of the spectra is produced, where the darkness of the film is proportional to the power density at each frequency. A typical Rayspan record is shown in Figure 4. The commutator is such that filters are sampled in groups of three giving effectively a band of 418 inverse phased triplets. To study the frequency range of 0-2.5 KHz, the input VLF data is played

back at four times real time. Under this condition, the nominal characteristics of the system are:

Effective bandwidth of a single filter	=	10 Hz
Average spacing of single filters	=	6.25 Hz
Attenuation outside bandwidth of single filter	=	6 dB/octave bandwidth
Attenuation outside bandwidth of three filter set	=	18 dB/octave bandwidth
Clear to black dynamic range of 35 mm. film	=	12 dB.

The actual operation of the instrument has been found to be far from ideal. Main sources of error are the variations in shape of the response curves of each of the filters, unequal spacing between the center frequencies of adjacent filters, and the limited dynamic range of the film. These problems lead to errors, in the measurement of noise band cutoff frequencies, as great as 40 to 50 Hz. However, the method does provide a means of obtaining, with good time resolution, a quick synoptic view of the VLF noise.

3.1.2 The Sonograph

The Sonograph (made by Kay Electric Co.) also produces a display of the VLF signal in the frequency versus time format, with amplitude of noise proportional to the darkness of the paper. The principle of its operation consists of recording 2.4 seconds of the VLF signal on a magnetic drum; this re-recorded signal is then played back repeatedly through a single filter. The center frequency of the filter is slowly increased by mechanically varying the resistance. Output of the filter causes electro-sensitive paper to be darkened on a linear scale. For use in analyzing relatively low frequencies (ELF), the input data is played onto the magnetic drum at four times real time, giving 9.6 seconds of data on the drum and a frequency display from 0 to 1.75 KHz. The effective bandwidth of the filter is 11 Hz with skirt attenuation 10-15

dB/octave bandwidth. Dynamic range of the paper covers about 5-8 dB. Results of this type of analysis are shown in Figure 6.

The Sonograph has several advantages over the Rayspan which are not immediately apparent from the specifications. Chief amongst these is that a single filter is used. Thus problems of non-uniform response of different filters, as is the case for the Rayspan, are eliminated. Also, since the center frequency is easy to vary in a uniform manner, uneven filter spacing problems are avoided. However, the dynamic range of the instrument is significantly less than for the Rayspan. Also it takes about 10 minutes to analyze 9.6 seconds of data, whereas the Rayspan can run at four times real time.

When trying to measure the frequency of a sharp lower cutoff of a noise band, one is still limited in practice to an uncertainty of about ± 25 Hz.

3.2 Digital Spectrum Analysis

In order to achieve greater frequency resolution than was previously available, and to obtain the actual shape of the power spectrum for ELF noise bands, a system for digital spectrum analysis was set up. It is desirable to analyze the noise over the frequency range from 70 Hz to 1 KHz with a resolution of 4 Hz. This was achieved; details of the analog/digital conversion and then the digital spectrum analysis are given in the following section. A synthesis of recent ideas in the field of digital spectrum analysis techniques is provided in the Appendix. Typical results of the analysis are shown in Figures 7 to 11.

3.2.1 Analog/Digital Conversion

Playback of the analog VLF signal for conversion to digital form is effected using an Ampex Model FR 104 tape recorder. Frequency response of the recorder is flat down to ~30 Hz and equalization problems between this recorder and the original (a Sangamo Model 4712) are negligible.

The block diagram in Figure 2 illustrates the basic arrangement whereby the analog VLF signal is converted to an equivalent binary representation on magnetic tape. Sampling rate of the A/D is controlled by an external pulse generator which is 'AND'-ed with the computer.

The signal from the analog tape recorder is amplified to a level compatible with full use of the A/D input range, and then band-pass filtered to reduce the effects of 'aliasing' (see Appendix) and to keep out any large quasi-D.C. components. Skirt attenuation of the filter is 20 dB per octave.

Conversions are performed by a Texas Instruments Inc. Model 846E Analog-Digital-Analog Converter. Aperture time is 0.1 sec., input dynamic range ± 8.19 volts, and output the 12-bit (including sign) binary equivalent. Sampling rates up to ~50 KHz may be achieved.

A 'machine language' program for control of the A/D has been written for the CDC 3200 computer†. The following operations are performed:

(1) Blocks of N samples are buffered into core memory from the A/D converter. Samples are stored in memory until the block of N is completed and then transferred to digital magnetic tape.

(2) M blocks of the above length N are taken with no intervening gaps.

---

†The program was provided by Mr. Scott Inrig of the D.R.T.E., Ottawa.

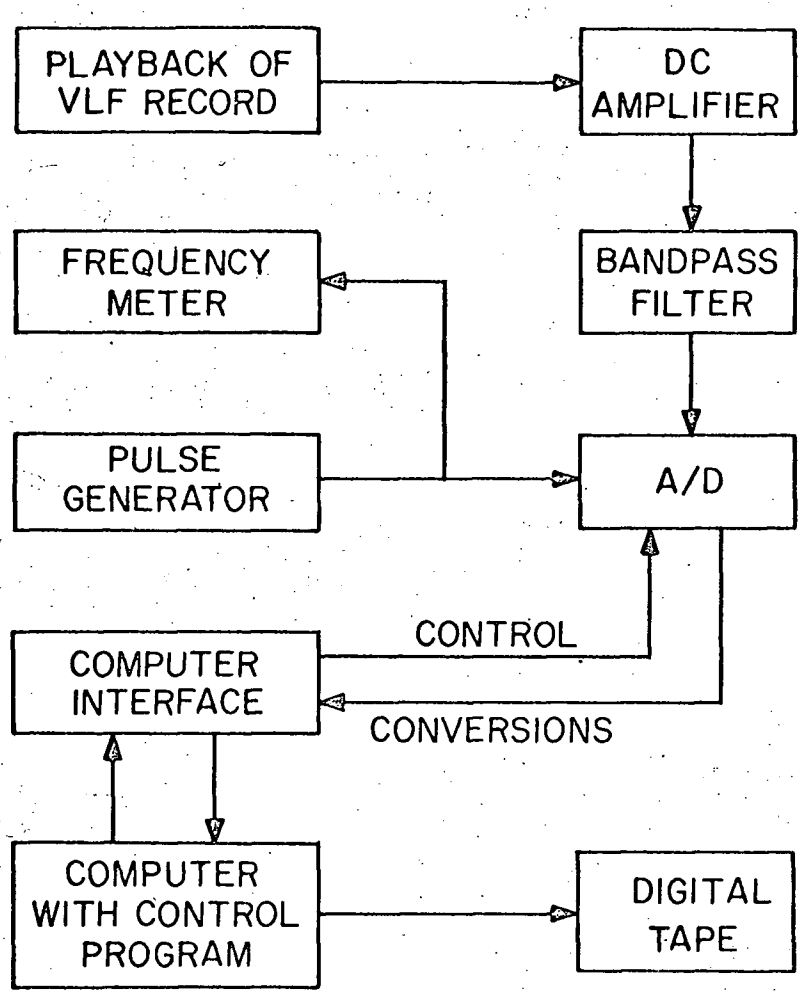

Fig. 2. Block diagram of the equipment setup used for digitization of the VLF analog records.

(3) Each set of M blocks is taken beginning at T sec. intervals. Clearly,

$$M \cdot N \cdot (1/\text{sample rate}) < T.$$

For analysis of the ELF noise bands, eight or twelve blocks of 2048 samples each were taken commencing each 60 seconds, and at a sample rate of 4,000 samples/second. In practice, it is possible to increase playbacks of the VLF signal to 2 or 4 times real-time, along with corresponding adjustments to filter frequencies and sample rates.

3.2.2 Digital Spectrum Analysis

In this section an outline will be given of the spectrum analysis of the digitized data (for details refer to the Appendix). Briefly, modified power spectrum estimates are constructed for each block of 2048 samples. Results of spectrum analysis of 8 (or 12) blocks are then combined.

A block of samples is designated:

$$X_0, X_1, \ldots X_{2047}.$$

This data is Fourier transformed according to

$$a_r + ib_r = \sum_{k=0}^{2047} X_k \, e^{-2\pi ik\left(\frac{r}{N}\right)}$$

$$r = 0,1,1,\ldots, 1024,$$

using a 'fast Fourier transform' routine†. The Fourier coefficients $(a_r + ib_r)$ are transformed by 'hanning' (equation A-17, Appendix) to reduce 'leakage', thus obtaining the modified Fourier coefficients:

$$A_r + iB_r \;, \; r = 0,1,2,\ldots, 1024.$$

Modified power spectrum estimates are then

---

†Program written by Mr. R.W. Herring of the D.R.T.E., Ottawa.

$$P_r = A_r^2 + B_r^2 \ , \ r = 0,1,2,\ldots, 1024,$$

where normalization has been neglected. Averages are then taken over the 8 (or 12) blocks in a set:

$$P_{r_{avg}} = \frac{P_{r1} + P_{r2} + \ldots + P_{rM}}{M}$$

where, M = the number of blocks per set. This represents a time average of 4 (or 6) seconds. These power estimates have statistical stability (for an approximately stationary gaussian process) corresponding to a 'chi-square' distribution of 16 (or 24) degrees of freedom. Reference to tables of this distribution (c.f. Blackman and Tukey, (1959)) shows that 80% of the estimates should deviate from the average value by no more than:

± 4 dB for 16 degrees of freedom
± 3 dB for 24 degrees of freedom.

For purposes of analyzing a steady noise band, 8 blocks of data per set suffices when whistler activity is low. The whistlers represent a non-stationary perturbation of the noise spectrum. For moderate whistler activity, 12 blocks per set were used.

Although the shape of the effective filter used in this type of analysis is theoretically known from the spectral window for the 'hanning' process (Figure 19 in the Appendix), an experimental determination of its shape was performed by generating a 400 Hz cosine wave for eight blocks of data. The cosine function for each block was displaced by $2\pi/10$ radians, thus allowing an estimation of the average effects of finite length records to be included. Results of spectrum analysis of this data are shown in Figure 3. Characteristics of the effective filter are:

bandwidth ~ 3.12 Hz
skirt attenuation ~ 28 (dB/octave bandwidth) down to 40 dB.

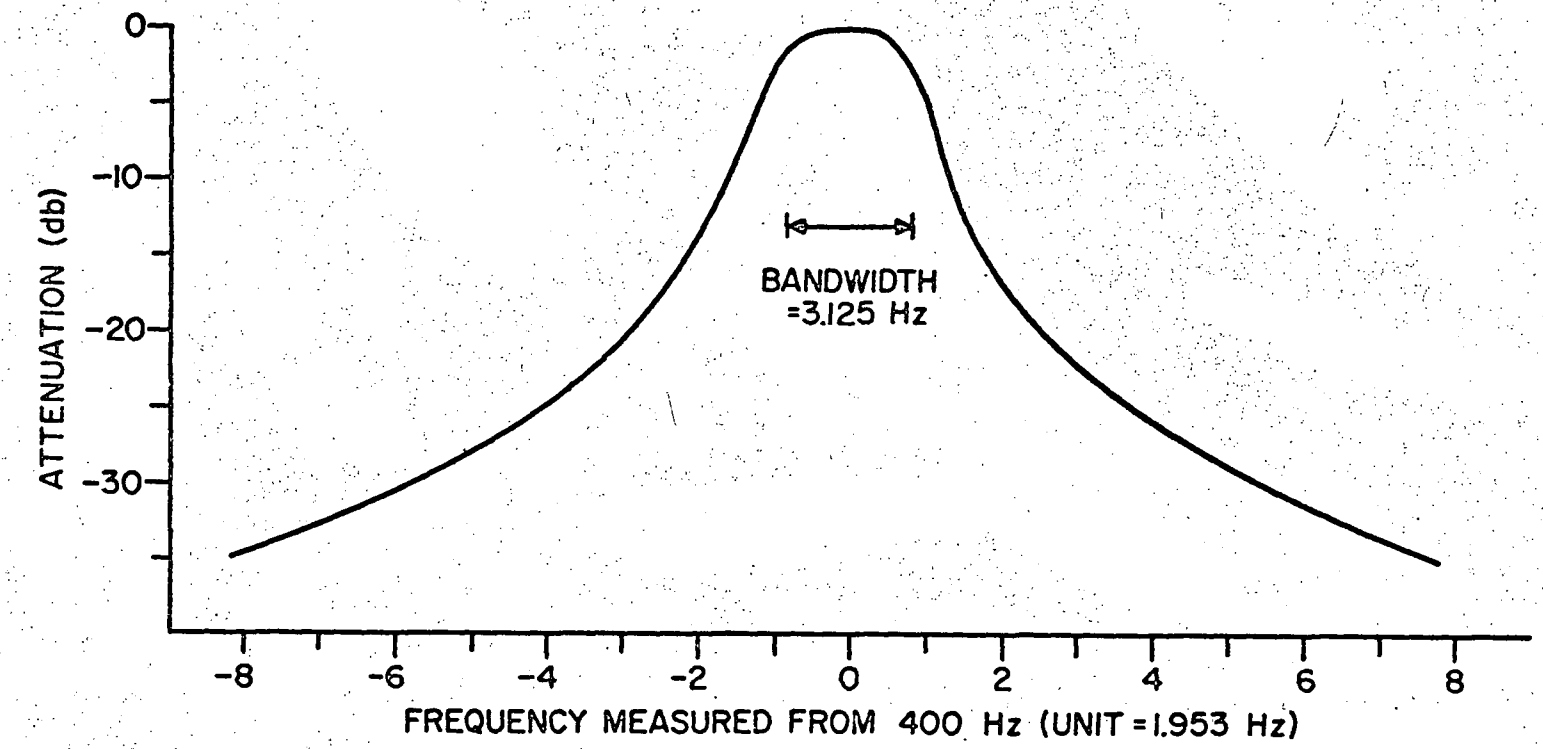

Fig. 3. Effective filter of the digital spectrum analysis program. Bandwidth is 3.125 Hz and skirt attenuation down to -40 dB is 28 dB/octave bandwidth.

Thus, the frequency at which a sharp cutoff occurs can be measured to within ± 4 Hz. Other possible errors in the analysis are:

flutter in tape recorders (± .5%)
inaccuracy in sample rate (± .2%).

Therefore, the maximum error in determining a cutoff frequency near 500 Hz is ± 7.5 Hz.

A plotter routine was written to output results of the spectrum analysis. Using a CDC 3200 computer, the time required to produce the modified power spectrum averaged over 8 blocks of data is 19 seconds. An additional 21 seconds is required for each plot routine.

3.3. Discussion

For the morphology of the ELF noise bands, and the selection of satellite passes for further analysis, Rayspan analysis is quite suitable. This method has the advantage over digital techniques of giving spectra continuously with time, and can be performed at rates four times faster than the real-time acquisition of the data. A synoptic view of the VLF activity in each pass is easily and quickly obtained. However, estimates of cutoff frequency of a noise band obtained from Rayspan records were found to be in error by as much as 50 Hz.

The Sonograph has greater frequency resolution than the Rayspan, but is still not sufficient to locate a lower frequency cutoff to better than 25 Hz. Further difficulty arises from its relatively low dynamic range.

The digital analysis does not give the comprehensive view of the noise band obtained from continuous (analog) analysis. However, the following advantages may be pointed out by way of comparison:

(a) integration in time and frequency can be widely varied to obtain the desired resolution and stability. For the analyses to be presented, the frequency resolution is adjusted to ~ 3 Hz. The analog system does not have resolution much greater than 25 Hz;

(b) the digital analysis gives a quantitative picture of the relative power density versus frequency. This power is measured from the system noise level. Analog white-to-black presentations only indicate qualitatively the shape of the spectrum. Furthermore they are limited to a 6-12 dB dynamic range;

(c) the effective digital filter has greater skirt attenuation than the analog methods. This is especially important when measuring a noise band with a steep 20 dB cutoff.

3.4 Sharpness of Cutoffs

Often in the literature, one sees references to the cutoff frequency of a noise band, and this cutoff is classified as either sharp or diffuse. When using analog analysis, this is a visual statement, in that sharp cutoff refers to an abrupt change from black to white, representing a similar decrease in power over a small range of frequency. Thus the noise band in Figure 4 has sharp lower frequency cutoff, whereas that in the bottom Sonogram of Figure 6 has a diffuse cutoff.

As part of the investigation of ELF noise bands, a large amount of Rayspan data was examined, and the upper and lower frequency cutoffs of bands near the gyrofrequency were classified as 'sharp', 'almost sharp', or 'diffuse'. Scale of the Rayspan data was 0 to 2.5 KHz on the vertical

(transverse to the film) axis and 1" = 4 sec. horizontally.

From observations of the Rayspan data and corresponding digital analysis results, it is possible to determine what is called a 'sharp' or 'diffuse' cutoff. The definitions listed in Table 2 were used for classification of the analog data, and also may be applied to the digital spectra.

TABLE 2

SHARPNESS OF CUTOFFS

Sharp:	$\gtrsim$ 5 dB in 25 Hz
Almost Sharp:	$\lesssim$ 5 dB in 25 Hz & $\gtrsim$ 10 dB in 100 Hz
Diffuse:	< 10 dB in 100 Hz

CHAPTER 4

RESULTS OF DATA ANALYSIS

4.1 Particular Characteristics of the Noise Band

Spectrum analysis results, displaying most of the particular characteristics of the ELF noise band, are shown in Figures 4 to 11. The Rayspan records (Figures 4 and 5) are typical examples of the noise band spectra, showing that the main features vary only slowly in time. Under each of these records, the corresponding AGC level is indicated in decibels of noise into the VLF receiver. Sonograms of structure, which occasionally appears on the noise band, are displayed in Figure 6. The results of digital spectrum analysis of five Alouette II passes are presented in Figures 7 to 11. These latter passes were preselected only on the basis that Rayspan data indicated a sharp lower frequency cutoff over part of each satellite pass, and that they represent a wide variety of latitudes and altitudes. On each spectrum the Greenwich Mean Time (GMT), calculated proton gyrofrequency (Ωp), angle between the velocity vector of the satellite and the geomagnetic field ($\angle (\vec{V},\vec{B})$), height, and invariant latitude (Λ, as defined by O'Brien et al., (1964)), respectively, are indicated. Also on each spectrum, arrows locate in frequency one or two prominent features. When the cutoff is sharp, the indicated frequencies are measured at the top of the cutoff. In the absence of such cutoffs the arrows locate relatively large fluctuations in the spectrum or merely the position of the gyrofrequency. The drop in noise level below 70 Hz is due to the pre-filtering of the data mentioned in Section 3.1. Each spectrum has been independently normalized.

There exists uncertainty with respect to the calculated parameters of the satellite and magnetic field. The absolute position of the satellite

is known to within ~ 3 Km. (G.E.K. Lockwood, personal communication). The magnetic field model used in calcuation of the proton gyrofrequency and $\angle(\vec{V},\vec{B})$ is GSFC, 9/65 (Hendricks and Cain, (1966)). These authors indicated a maximum error of ± 200 γ in total field, corresponding to ~ 3 Hz in proton gyrofrequency. A more exhaustive study of possible errors in geomagnetic field models (Cain et al., (1967), indicates that the standard error in declination and inclination angles at altitudes of 1,000 Km. is (on a world wide basis) approximately .3° and .07°, respectively. These standard errors will probably be larger near the magnetic poles, due to the scarcity of magnetic data in these regions. Thus, errors in $\angle(\vec{V},\vec{B})$ of ± 3°, as a result of uncertainty in the direction of the geomagnetic field, are quite conceivable.

These sets of spectra will now be individually examined, and the characteristics of the noise band along with associated orbital features, discussed.

Figure 7 is from a low altitude satellite pass covering low and mid-latitudes. The sharp lower frequency cutoff of the noise band follows the calculated proton gyrofrequency to within 3 Hz. During part of the pass (GMT 2128 to 2131) the noise band is not visible. This time corresponds to very low latitudes, and also $\angle(\vec{V},\vec{B}) \sim 0°$ (i.e., the satellite is travelling nearly parallel to the geomagnetic field). Note that the noise band has an upper frequency cutoff from GMT 2133 to 2137, and this frequency is below twice the proton gyrofrequency.

Figure 8 also covers mid-latitudes but at altitudes near satellite apogee. Lower frequency cutoffs are approximately 20 dB in 25 Hz. The low frequency side of the cutoff occurs within 30 Hz of the calculated gyrofrequency. The upper frequency cutoff is near three times the proton gyrofrequency and there is some evidence of a change in noise level near

twice the gyrofrequency. At such high altitudes the satellite is, most probably, well into the protonosphere (Hoffman, (1969)).

The next two figures (9 and 10) cover the high latitudes at very high satellite altitudes. Observations on these spectra are: (a) above $\Lambda = 78°$, harmonic structure on the noise band is evident; (b) the noise band has a progressively less sharp lower cutoff frequency above $\Lambda = 79°$; (c) at satellite positions where $\angle(\vec{V},\vec{B}) \sim 90°$, the noise band is not well defined.

Figure 11 shows spectra from a low altitude, mid- and high-latitude satellite pass. The lower cutoff frequency generally lies from 5 to 15 Hz below the calculated gyrofrequency. The result of Rayspan analysis of this same pass is shown in Figure 5. By comparing these two figures, it is seen that there are two effects which may be associated with $\angle(\vec{V},\vec{B})$ going through 90°. The noise with lower frequency cutoff near the gyrofrequency is increasingly smeared out as $\angle(\vec{V},\vec{B}) \to 90°$; and another noise band comes down from higher frequencies, crossing over to the very low frequencies. Similar effects are seen on the noise band in Figure 4.

The smearing out of the noise band when $\angle(\vec{V},\vec{B}) \sim 90°$ was further investigated, by calculating $\angle(\vec{V},\vec{B})$ throughout 230 satellite passes. Thirty passes were found where this angle passed through 90°, and Rayspan data indicated that the noise band existed. In all these cases, the spectral characteristics of the noise exhibited a dependence on $\angle(\vec{V},\vec{B})$. Typical of this dependence is growing down of noise below the lower frequency cutoff, and cutoffs which become diffuse, when the angle between the velocity vector of the satellite and the geomagnetic field is near 90°.

Another observation on this noise band is shown in Figure 6. These Sonograms, also taken from the satellite pass of Figures 4 and 11, show

structure in the form of rising tones superimposed on the noise band. This structure is seen only occasionally for satellite passes from invarient latitudes of approximately 50° to 70°, and is typically characterized by a lower frequency cutoff near the proton gyrofrequency.

An additional observation on this noise band is a marked decrease in noise band intensity (~ 10-20 dB) which occurs twice per spin period when the spin axis of the satellite is nearly perpendicular to the geomagnetic field. This phenomenon is termed 'spin modulation'. Comparison of the spin modulation times with data from the three-component magnetometer aboard the satellite, indicated that (within an accuracy of ± 15°) the intensity nulls occurred when the VLF antennas were aligned with the geomagnetic field.

4.2 General Occurrence Pattern of the Noise Band

Rayspan data for approximately 75 hours of Alouette II VLF data has been examined. The satellite passes, each about 20 minutes long, were primarily from the northern hemisphere and of epoch 1966. At 4 to 5 minute intervals during each pass the occurrence or non-occurrence of the noise bands near the proton gyrofrequency was noted, giving a total of 971 observations. When the band occurred the upper and lower frequency cutoffs were classified as sharp, almost sharp, or diffuse according to Table 2.

There exists some question as to whether the noise band still exists although it is not seen in the Rayspan data. If very intense noise occurs at frequencies other than in the ELF band, the AGC will desensitize the receiver thus making it more difficult to see the ELF noise band in the Rayspan (0-2.5 KHz) record. It has been noted in section 2.1 that a 12 dB change in receiver input only effects a 1 dB

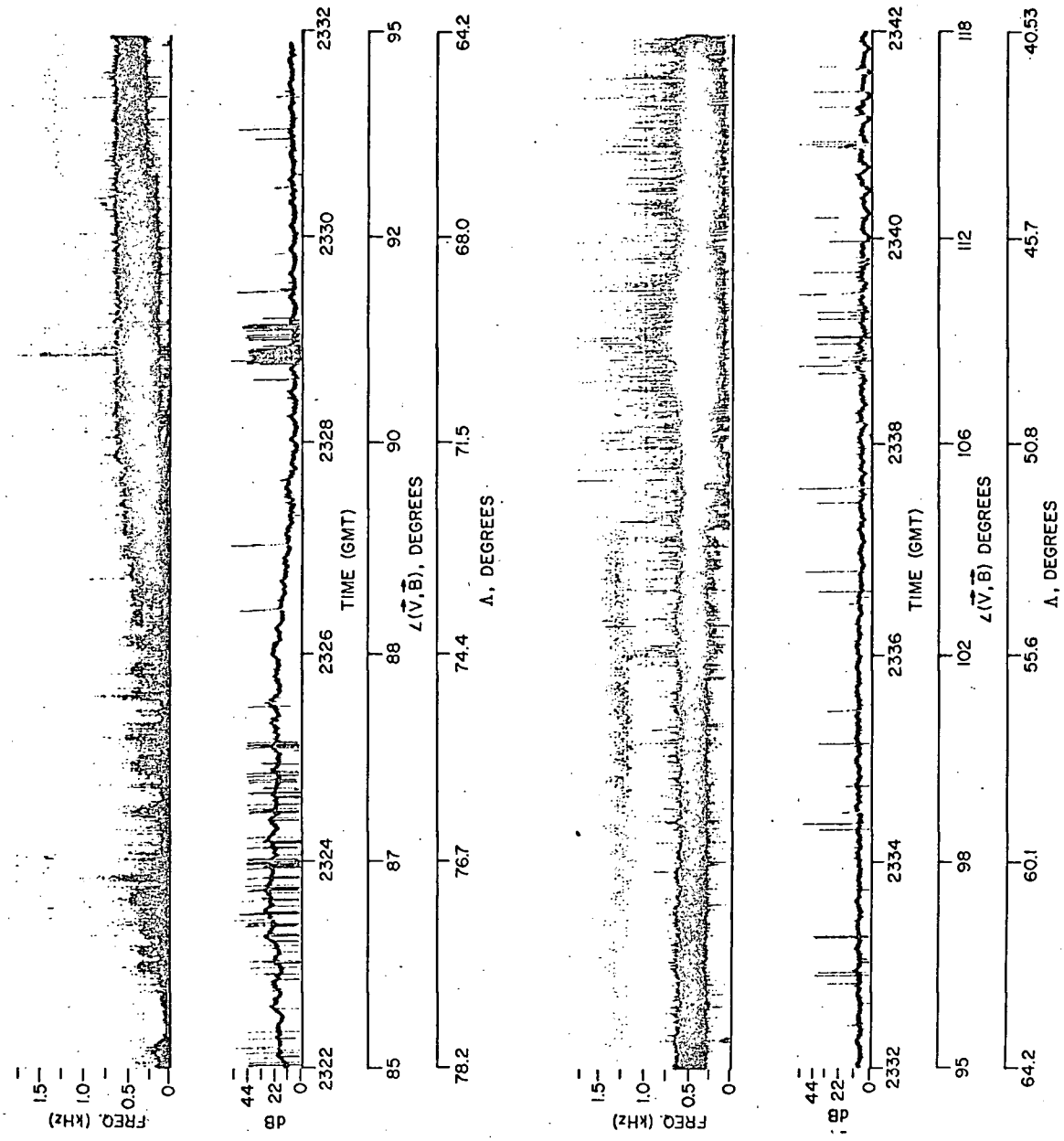

Fig. 4. A 'Rayspan' spectrogram from the Alouette II VLF receiver on July 23, 1966. AGC level, time, angle between the velocity vector of the satellite and the geomagnetic field, and invariant latitude are indicated below and each portion of the spectrogram. Digital spectrum analysis of this pass indicated a sharp lower frequency cutoff from 2328 GMT. These cutoff lay <20 Hz below the calculated proton gyrofrequency.

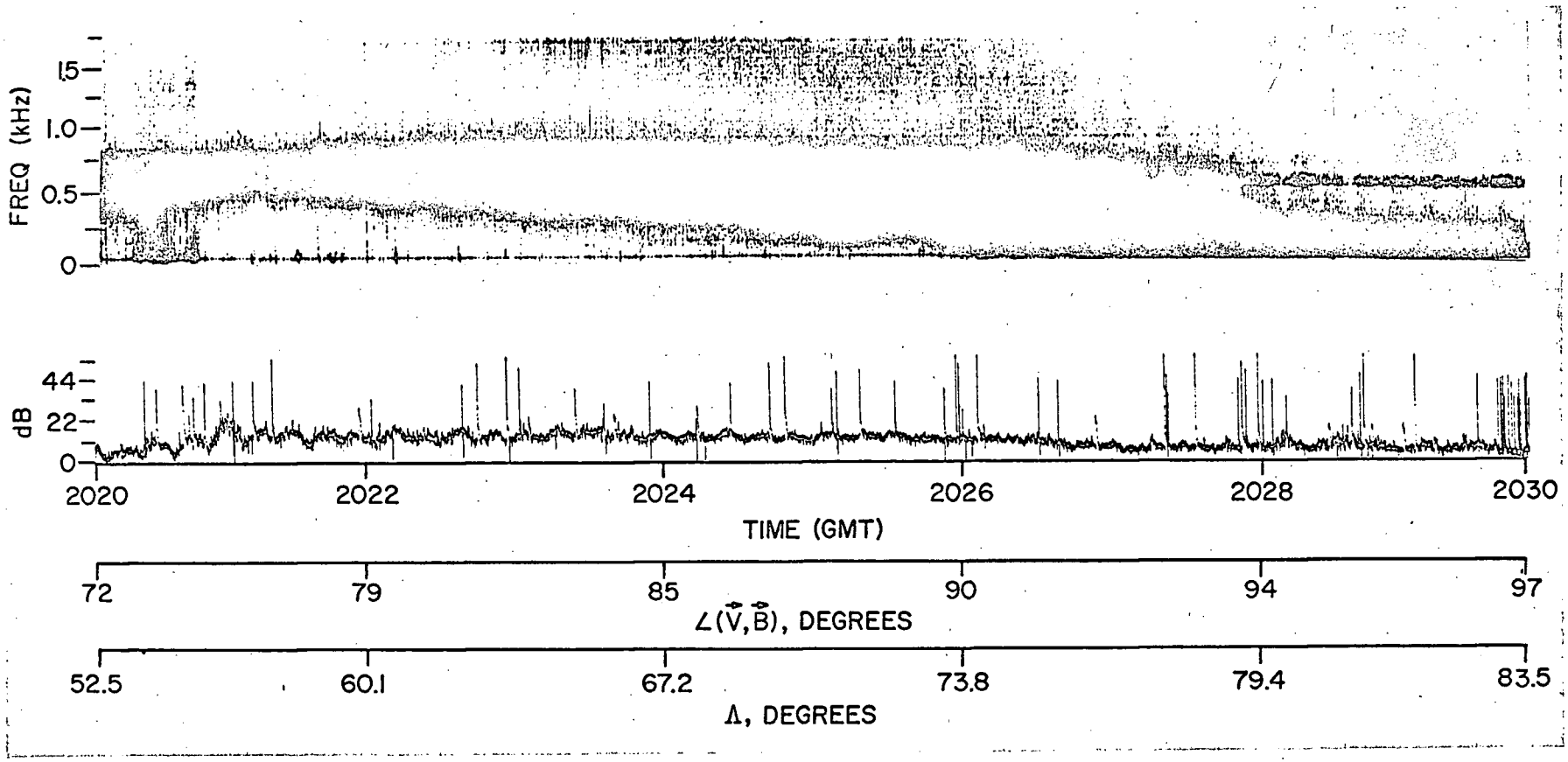

Fig. 5. A 'Rayspan' spectrogram from the Alouette II VLF receiver on May 13, 1966. Digital spectra for the same pass are presented in Figure 11.

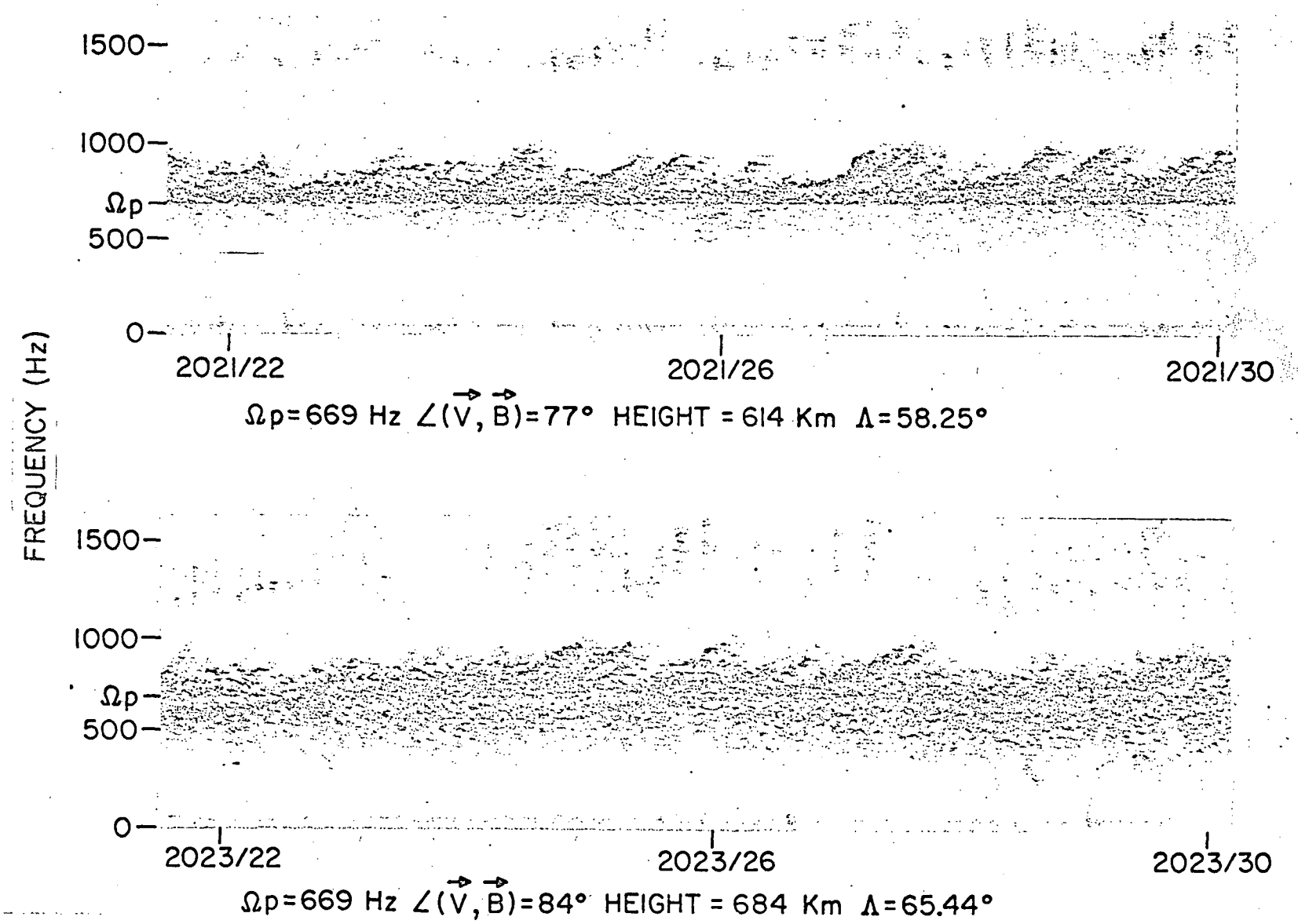

Fig. 6. 'Sonograms' from a mid-latitude pass on May 13, 1966. Structure in the form of rising tones is seen superimposed on a noise band which has a lower frequency cutoff near the proton gyrofrequency. Spectra from the same pass are shown in Figures 5 and 11.

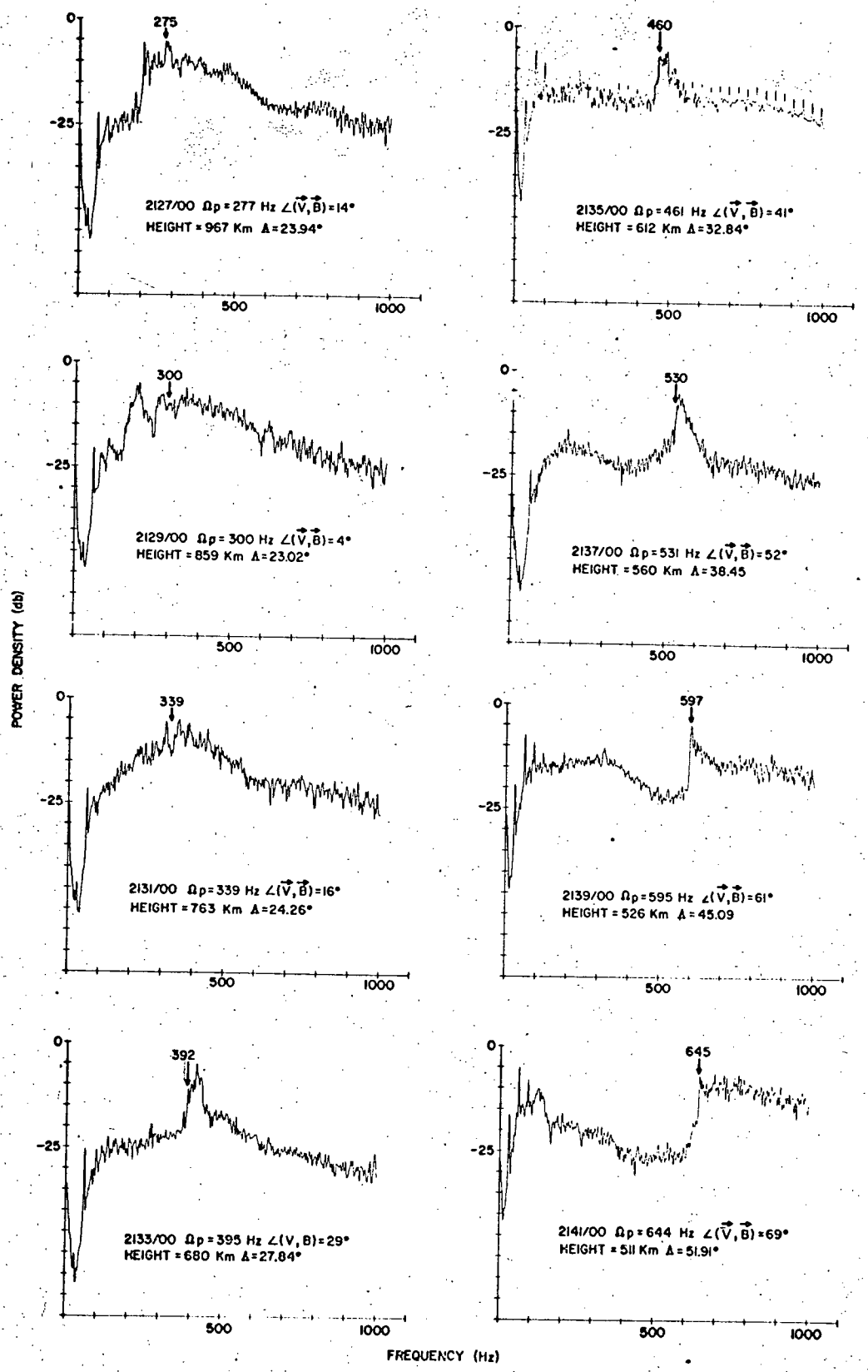

Fig. 7. Digitally computed spectra for a low altitude, low and mid-latitude pass on November 7, 1966.

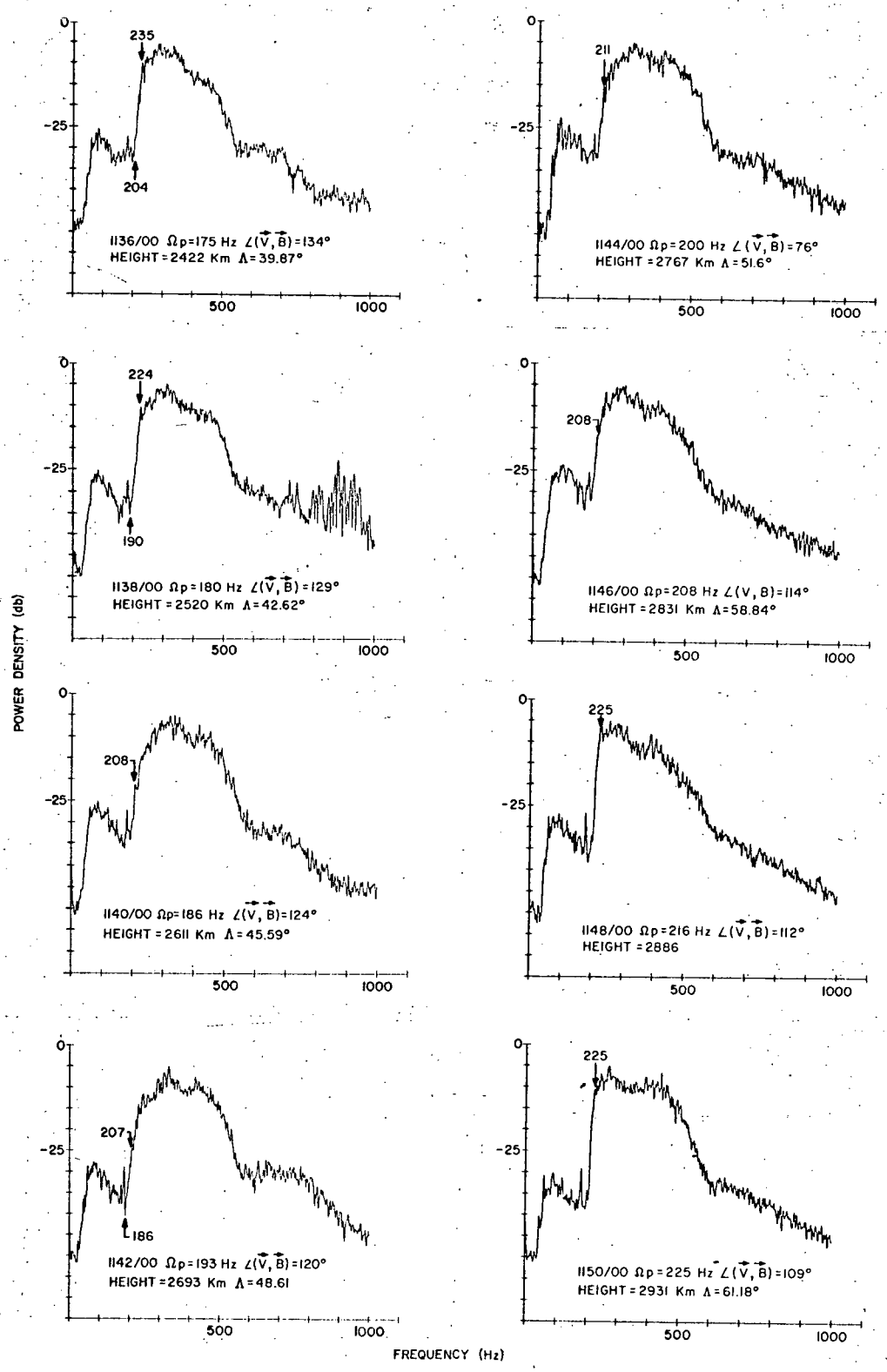

Fig. 8. Digitally computed spectra from a high altitude, mid-latitude pass on October 14, 1966.

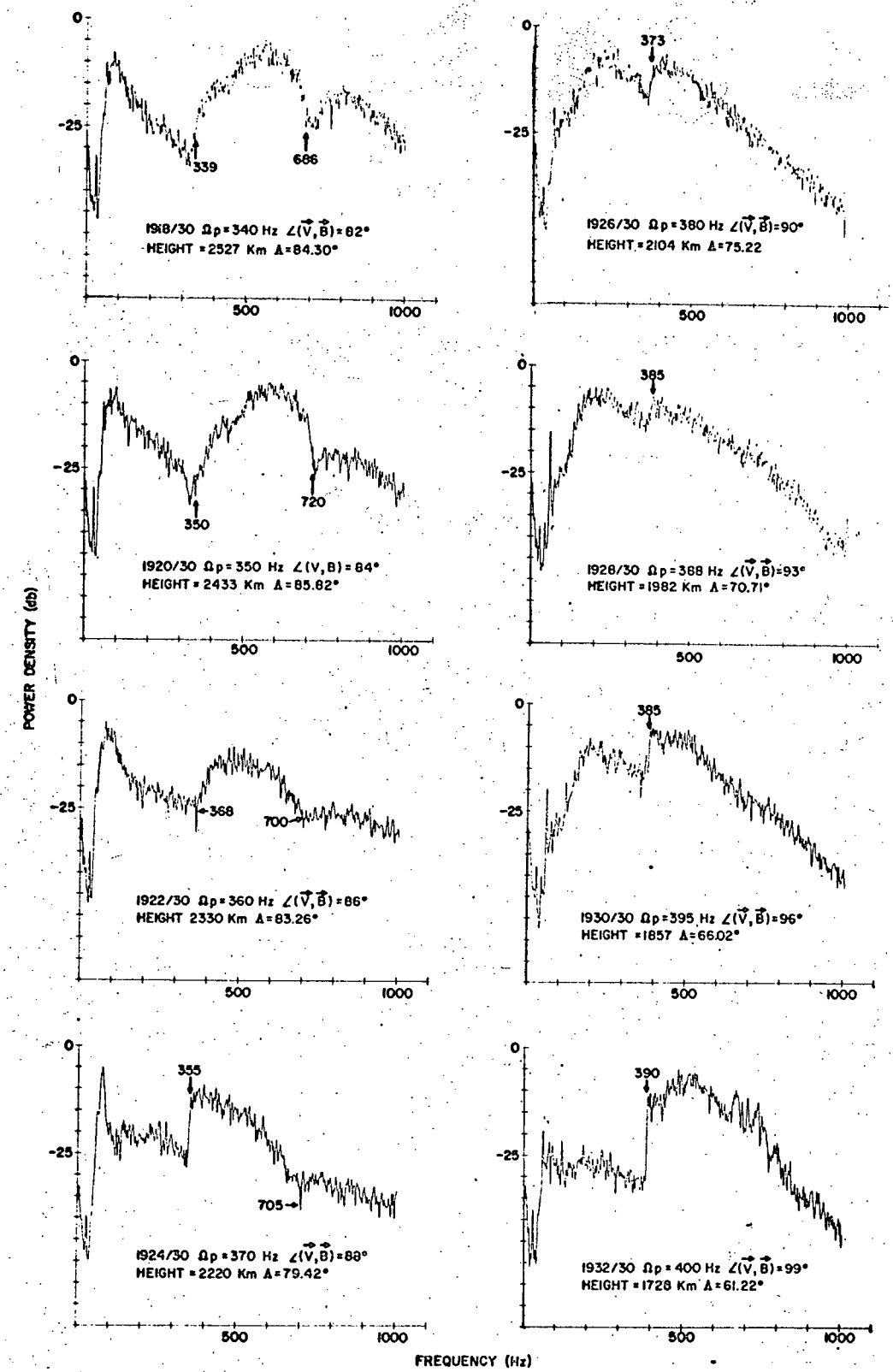

Fig. 9. Digitally computed spectra from a high altitude, high latitude pass on July 30, 1966.

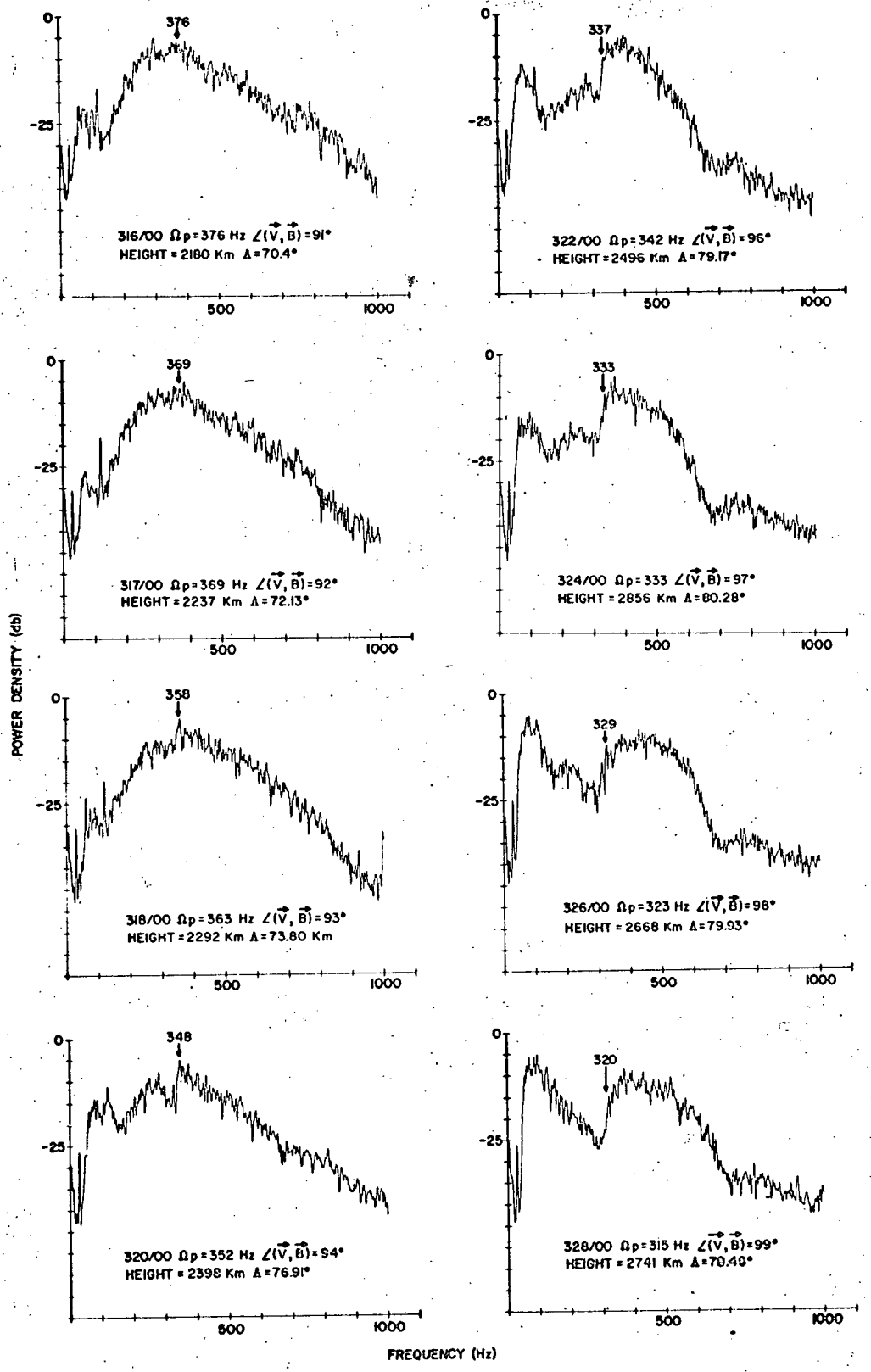

Fig. 10. Digitally computed spectra from a high altitude, high latitude pass on June 13, 1966.

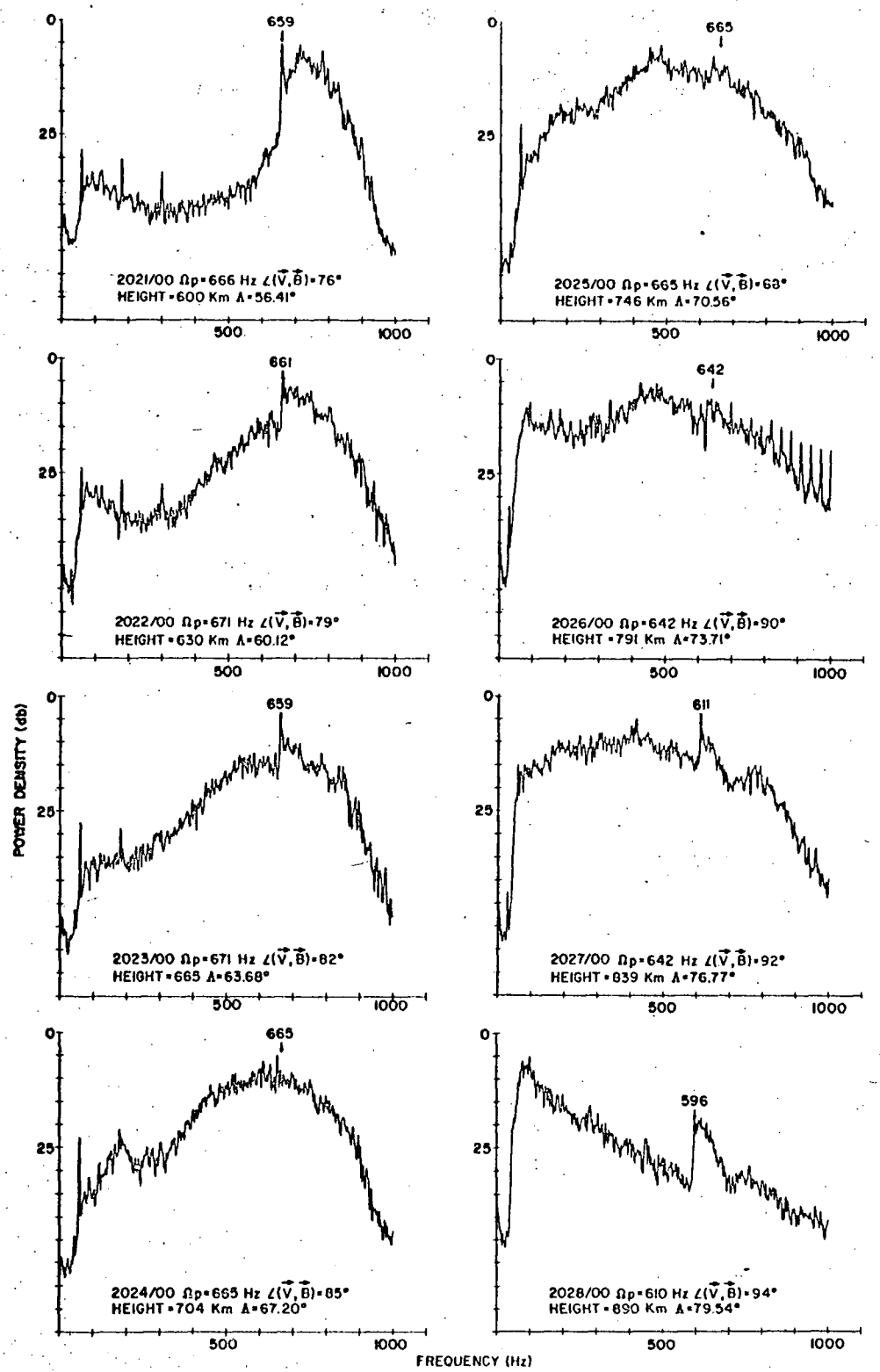

Fig. 11. Digitally computed spectra from a low altitude, high latitude pass on May 13, 1966.

change in receiver output. If it is the ELF noise band which controls the AGC, then the Rayspan (which has a 12 dB clear to black range) is capable of covering an input range of ~ 72 dB. However, if large signals, at frequencies other than in the ELF band, enter the receiver system, then receiver gain may be sufficiently reduced so that the band is no longer visible in the Rayspan record. Thus a region of observed non-occurence of the noise band may only represent a region of high signal strength at frequencies other than in the ELF range. A saving feature is that the distribution of AGC levels in invariant latitude and local mean time (Barrington and Harvey, (1969)) shows high AGC levels only at times when the ELF noise-band occurrence is high. Therefore, one may infer that AGC degredation of receiver gain cannot have substantially influenced the final ELF noise band occurrence pattern.

In analyzing occurrence patterns of a phenomenon observed by satellite, some care must be taken in choosing the independent variables. A peculiar problem which arises from the orbital characteristics of Alouette II is that (for epoch 1966) the satellite is generally at high altitudes on the night-time side of the earth and at lower altitudes on the day-side. That this can be so, for a full year, can be understood by examining the orbital elements of Table 1. It is seen that the argument of the perigee varies by 1.8922 degrees/day and this is closely matched by the variation of the longitude of the ascending node in the earth-sun system (- .7922°/day - 360°/year = - 1.7778°/day). Thus there exists a strong correlation between the local mean time (LMT) at the satellite and its altitude, and the concomitant ambiguity in the occurrence data being analyzed cannot be resolved. In the analysis which follows, LMT is taken as an independent variable, but the connection with altitude should properly be remembered.

Analysis of the data on occurrence and sharpness of cutoffs, was performed by entering this data into storage in the computer along with the corresponding world map data for the satellite (geomagnetic, and invariant latitude, local mean time, and the three hourly planetary magnetic index, Kp). The morphology results shown in Figures 12, 13 and 14 were obtained by sorting this merged data.

The percentage occurrence of the noise band as a function of local mean time and invariant latitude (Figure 12), is computed by counting the number of times the noise band is seen in each LMT (3 hr.) -- invariant latitude (10°) block, and dividing by the number of times the satellite is in the LMT -- invariant latitude block. These results were then contoured. Percentage occurrence of the sharp lower (and upper) frequency cutoffs in Figures 13a and 13b is calculated by obtaining the number of times there was a sharp cutoff of the band in each LMT (6 hr.) -- invariant latitude (10°) block and dividing by the number of times a noise band was observed in the block. The results shown in Figure 14 have been derived in a similar manner except that only Kp was subdivided.

Since the satellite generally goes through 10 degrees of invariant latitude within 4-5 minutes, then the results of each observation on the noise band, for any given pass, will be tabulated in a different cell of LMT -- invariant latitude space. Thus, Figures 12 and 13 are derived from 971 independent observations of the noise band. This is not the case for the Kp variations of Figure 14. Since Kp is constant for each pass, this figure represents averages over ~ 230 satellite passes.

Summarizing the results of Figures 12 to 14:

(a) The noise band appears, on the average, 57% of the time. There is a marked diurnal variation in the occurrence. Near

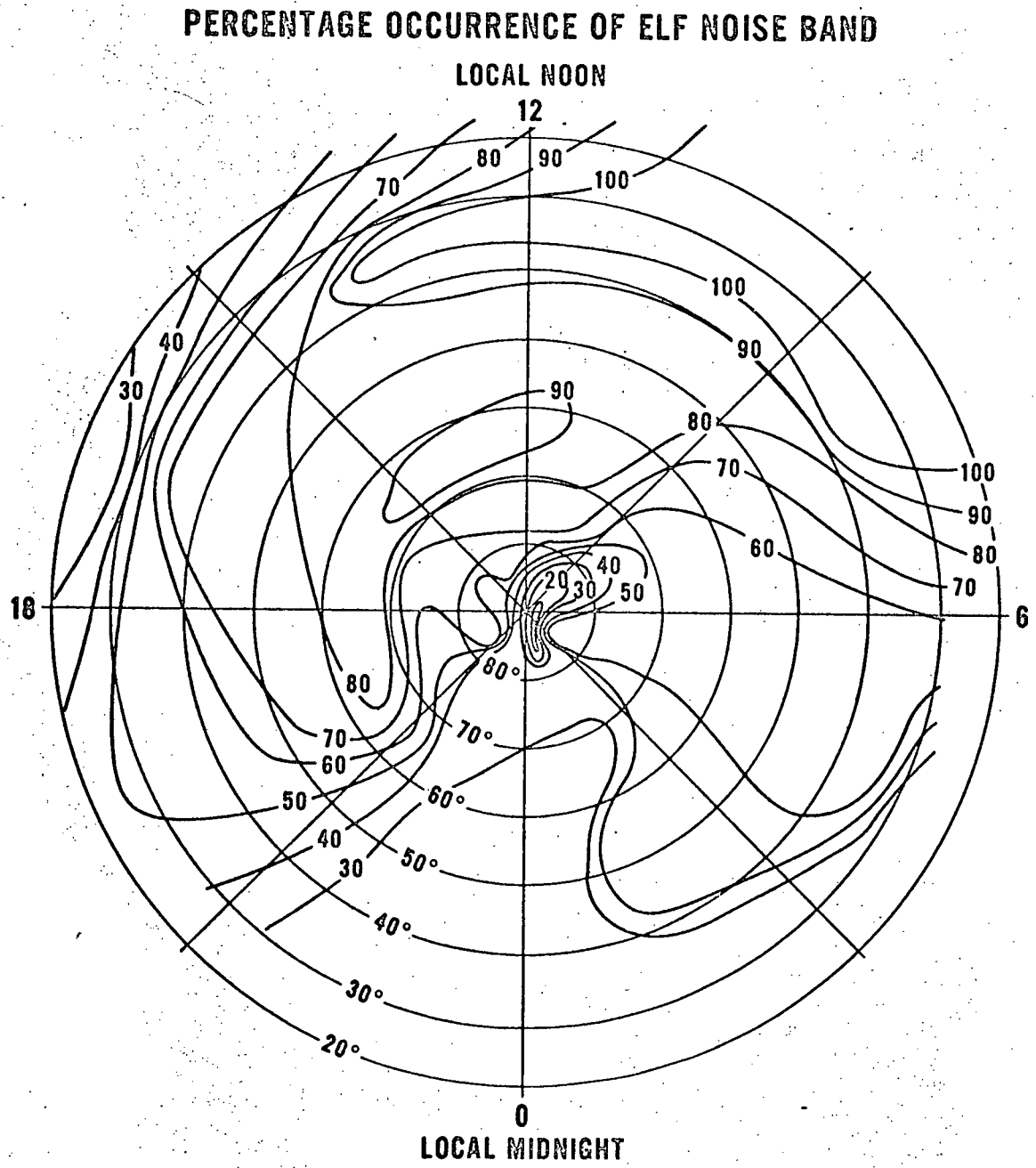

Fig. 12. Occurrence pattern of the noise band plotted as a function of invariant latitude and local mean time. Contours are in steps of 10% and give the percentage of the time the noise band was observed.

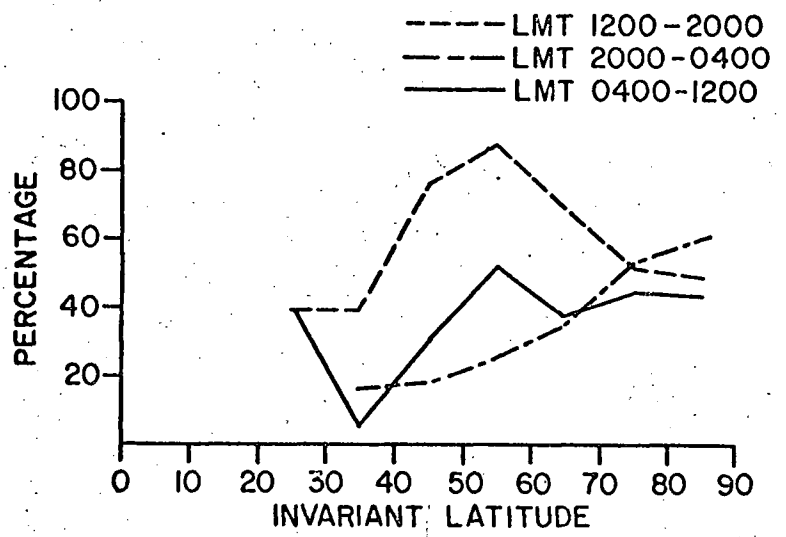

Fig. 13a. Occurrence of sharp lower frequency cutoffs as a percentage of the times for which the noise band was observed. This is plotted versus invariant latitude with local mean time as a parameter.

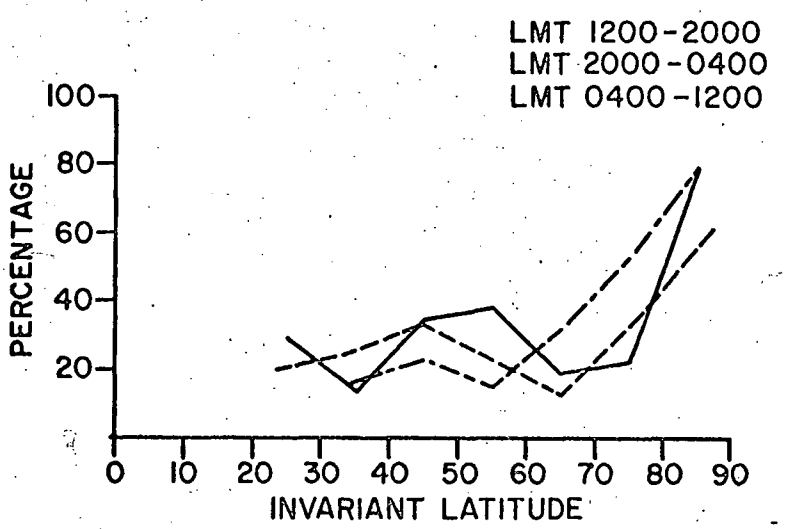

Fig. 13b. Occurrence of sharp or almost sharp upper frequency cutoffs as a percentage of the times for which the noise band was observed.

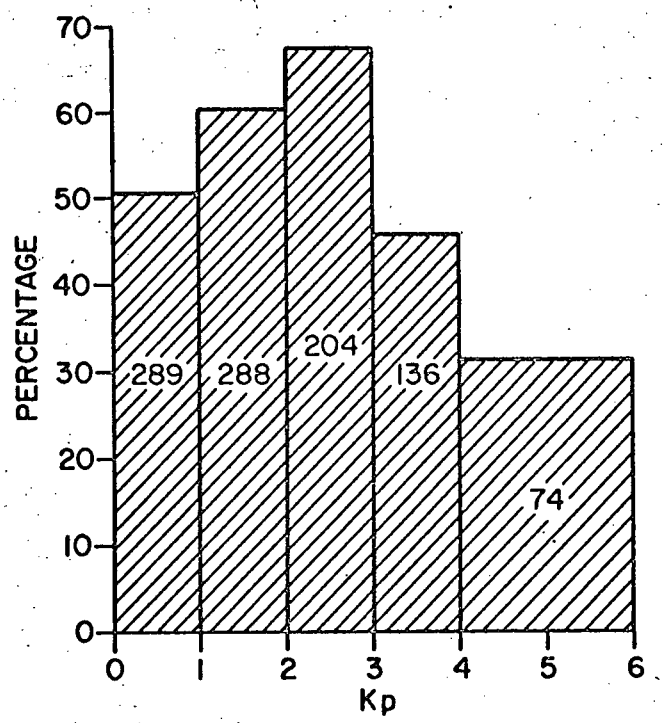

Fig. 14. The percentage occurrence of the noise band versus the three hourly planetary magnetic index K_p. Numbers within the hatches are the number of observations in each block of K_p.

dawn, occurrence is highest (100%) at the low latitudes. The zone of maximum occurrence broadens to higher latitudes by noon, and has a maximum at 60° - 70° invariant latitude and LMT 12 to 16 hours. Occurrence abruptly decreases near dusk.

(b) The occurrence of sharp lower cutoffs as a percentage of noise bands observed follows a pattern similar to (a). Occurrence is generally higher during the local daytime (associated with low altitudes).

(c) Occurrence of sharp (or almost sharp) upper cutoffs occurs most often at very high latitudes, and shows little dependence on LMT (or, what is the same thing, on altitude).

CHAPTER 5

THEORY OF PROTON CH WAVES

Quite comprehensive numerical studies have been made for the dispersion of electrostatic electron CH waves. To date though, no extensive numerical results have been reported for the proton CH waves. This is partly due to the fortunate circumstance that, for waves propagating perpendicular to the ambient magnetic field, results derived for electron CH waves at frequencies of the order of the electron gyro-frequency (Ωe) can be applied almost directly to proton CH waves at frequencies $\ll \Omega e$. The following will include a derivation of the isomorphism between the proton and electron CH dispersion relations with considerations of the effect on this isomorphism of small deviations from perpendicular (i.e., oblique) propagation. The literature on perpendicular and oblique propagation, and effects of collisions, for electron CH waves will then be reviewed, and the results applied to proton CH waves. A few remarks on instability in these modes will be added.

To show the equivalence that can be set up between proton and electron CH waves, the general dispersion relation for electrostatic waves (Stix, (1962)) is used. In a magnetized by-Maxwellian plasma, this is

$$k_{\perp}^2 + k_{11}^2 + \sum_j \frac{\pi_j^2}{\Omega_j^2} D_j = 0 \tag{5.1}$$

where

$$D_j \equiv \sum_{n=-\infty}^{+\infty} \frac{\pi_j^2 \, m_j \, e^{-\lambda_j} \, I_n(\lambda_j)}{\kappa \, T_{\perp}(j)} \cdot A_{nj}$$

$$A_n \equiv \frac{T_{\perp}}{T_{11}} + i \left[\frac{(\omega - k_{11} V_{11} + n\Omega) T_{\perp} - n\Omega T_{11}}{k_{11} T_{11}} \left(\frac{m}{2\kappa T_{11}} \right)^{\frac{1}{2}} \right] F_o(\alpha n)$$

$$F_o(\alpha n) \equiv \pi^{\frac{1}{2}} \frac{k_{11}}{|k_{11}|} e^{-\alpha_n^2} + 2i\, S(\alpha n)$$

$$S(\alpha n) \equiv e^{-\alpha_n^2} \int_o^{\alpha n} e^{t^2}\, dt \text{ , the error function}$$

$$I_n(z) \equiv \frac{1}{\pi} \int_o^{\pi} e^{z \cos\theta} \cos(n\theta)\, d\theta \text{, the modified Bessel fctn.}$$

$$\alpha n \equiv \frac{\omega - k_{11} V_{11} + n\Omega}{k_{11}} \left(\frac{m}{2\kappa T_{11}} \right)^{\frac{1}{2}}$$

$$\lambda_j \equiv \frac{k_\perp^2 \kappa T_\perp}{\Omega^2 m} \sim (\text{gyroradius})^2/(\text{wavelength})^2$$

$$\Omega_j \equiv \left| \frac{Z_j e B_o}{mc} \right| \text{ , the gyrofrequency}$$

$$\pi_j^2 \equiv \frac{4\pi\, n_j\, Z_j^2 e^2}{m_j} \text{ , the plasma frequency ;}$$

and B_o is the ambient magnetic field; k_{11} and $k_\perp$ are the parallel and perpendicular wavenumbers and ω the frequency of a wave of the type

$$\vec{E}(\omega,\underline{k})\, e^{i(\vec{\underline{k}}.\vec{r} - \omega t)} \text{ ; } m_j \text{ , } T_\perp^{(j)} \text{, } T_{11}^{(j)} \text{ , } n_j \text{, } V_{11j} \text{, and } Z_j e$$

are respectively, the mass, perpendicular and parallel temperature, number density, parallel drift velocity, and charge, of the jth type of charged particle in the plasma; κ and c are the Boltzmann constant, and velocity of light. Units are cgs electrostatic.

In particularizing the general dispersion relation Eq. (5.1) to proton CH waves, the following assumptions are made:

$\omega \ll \Omega e$ (and therefore, $\alpha n_e \gg 1$ for $|n| \geq 1$) ,

$\lambda_e \ll 1$ (that is, the electron gyroradius is small with respect to a wavelength),

$V_{11\ p,e} = 0$ (there are no parallel drift velocities),

$T_{11}^{(e)} \sim T_{11}^{(p)}$ (the electron and proton parallel temperatures are of the same order).

The electron portion of the dispersion relation can then be calculated to first order in λ_e:

$$\frac{\pi_e^2}{\Omega_e^2} D_e = \frac{\pi_e^2 m_e}{\kappa T_{11}^{(e)}} \left\{ S'(\alpha oe) + i \pi^{\frac{1}{2}} \alpha oe\ e^{-\alpha oe^2} \right\}$$

$$+ \frac{\pi_e^2 m_e}{\kappa T_{\perp}^{(e)}} \lambda_e \left\{ \frac{T_{\perp}^{(e)}}{T_{11}^{(e)}} + \frac{T_{11}^{(e)} - T_{\perp}^{(e)}}{2} - \frac{T_{\perp}^{(e)}}{T_{11}^{(e)}} \left[S'(\alpha oe) + i\pi^{\frac{1}{2}} \alpha oe\ e^{-\alpha oe^2} \right] \right\} \tag{5.2}$$

For $\lambda_p < 1$, a similar expansion could be made for the proton portion of the dispersion relation. The factor $\{S'(\alpha oe) + i\pi^{\frac{1}{2}} \alpha oe\ e^{-\alpha oe^2}\}$ in the first order term of Eq. (5.2) may be neglected in comparison with the zeroth order term. Also,

$$\frac{\pi_e^2 m_e}{\kappa T_{11}^{(e)}} \sim \frac{\pi_p^2 m_p}{\kappa T_{11}^{(p)}}$$

and

$$\alpha oe = \frac{\omega}{k_{11}} \left(\frac{m_e}{2 \kappa T_{11}^{(e)}} \right)^{\frac{1}{2}} \sim \left(\frac{m_p}{m_e} \right)^{\frac{1}{2}} \alpha op .$$

The behaviour of $S'(z)$ for real z is

$$S'(z) = \begin{cases} -1.0 \text{ for } z = 0 \\ 0.0 \text{ for } z = .924 \\ 0.285 \text{ for } z = 1.502 \\ \sim \frac{1}{2z^2} \text{ for } z > 2 . \end{cases}$$

From this, it is seen for small deviations of k_{11} from zero, that

$$1 << \alpha oe << \alpha op .$$

Thus, for small k_{11} and $\lambda_p \lesssim 1$, the effect of the $\{S'(\alpha oe) + i\pi\, \alpha oe\, e^{-\alpha oe^2}\}$ term will be even greater than the corresponding proton term. As a result, it is expected that the effects of non-zero k_{11} (to be discussed) on proton CH waves will be more pronounced than in the corresponding electron CH case. Proceeding now to take the limit as $k_{11} \to 0$, $T_\perp \sim T_{11}$, then Eq. (5.2) becomes:

$$\frac{\pi_e^2}{\Omega_e^2} D_e \cong \frac{\pi_e^2\, m_e\, \lambda_e}{\kappa\, T^{(e)}} = \frac{\pi_e^2\, k_\perp^2}{\Omega_e^2} \tag{5.3}$$

Then Eqs. (5.1) and (5.3) may be combined to give

$$k_\perp^2 (1 + \pi_e^2/\Omega_e^2) \cdot \frac{\Omega_p^2}{\pi_p^2} = - D_p \tag{5.4}$$

The corresponding dispersion relation for electron CH waves (neglecting all ion effects) is

$$\Omega_e^2/\pi_e^2\, k_\perp^2 = - D_e \tag{5.5}$$

Note that the terms D_e and D_p contain no reference to particle density. Then it is seen that an isomorphism between Eqs. (5.4) and (5.5) may be set up as shown in Table 3. The frequency $\pi_{L.H.}$ is referred to in the literature as the lower hybrid resonance frequency.

TABLE 3

ISOMORPHISM BETWEEN ELECTRON AND PROTON DISPERSION RELATIONS

Electron CH waves		Proton CH waves
$\frac{\kappa\, T^{(e)}}{m_e}$	$\longleftrightarrow$	$\frac{\kappa\, T^{(p)}}{m_p}$
Ω_e	$\longleftrightarrow$	Ω_p
π_e	$\longleftrightarrow$	$\left(\frac{1}{\pi_p^2} + \frac{1}{\Omega_p \Omega_e}\right)^{-\frac{1}{2}} \cong \pi_{L.H.}$ (for $\pi^2 \gg \Omega_p^2$)

Dispersion curves for perpendicularly propagating electron CH waves have been computed by Crawford (1965). These curves, particularized to proton CH waves, are shown in Figure 15. These curves have been confirmed for electron CH waves by a number of experimenters using laboratory plasmas (Harp (1965); Mantie (1967)). Any small non-Maxwellian component will slightly alter the dispersion. The values of $\pi^2_{L.H.}/\Omega^2_p$ to be expected at satellite altitudes are in the range 100 to 300.

Summarizing these curves, it is seen that propagation can occur in modes between each harmonic of the proton gyrofrequency. The solutions of Eq. (5.4) for ω and k are pure real and therefore propagation is unattenuated in the perpendicular direction. Phase velocities in the first pass band ($\Omega p \leq \omega \leq 2\Omega p$) are of the order of the proton thermal velocity $v_{o\perp} \left[\equiv \left(\frac{K T_\perp}{m_p}\right)^{\frac{1}{2}}\right]$, which for satellite altitudes is in the range of 3-5 Km/sec. These curves also indicate that group velocity ($d\omega/dk_\perp$) will approach zero at the bounding harmonics of the gyrofrequency.

Tataronis, (1967) has presented an extensive study of perpendicular and oblique propagation of electron CH waves under Maxwellian and non-Maxwellian conditions. Figure 16a shows the dispersion for oblique propagation of proton CH waves (from Tataronis via Table 3). The important results here are that another set of modes is introduced (mode 2), and that both sets of modes are heavily attenuated for non-zero k_{11}. Decrease in energy for the first set of modes (directly related to the perpendicularly propagating mode) is ~ 10 dB per cyclotron period for propagation at angles only 5° off perpendicular. Attenuation of the second set of modes is even greater (~ 25 dB/cyclotron period). For this reason, CH wave propagation in the ionosphere most likely will occur only with wave normals nearly perpendicular to the geomagnetic field. It is

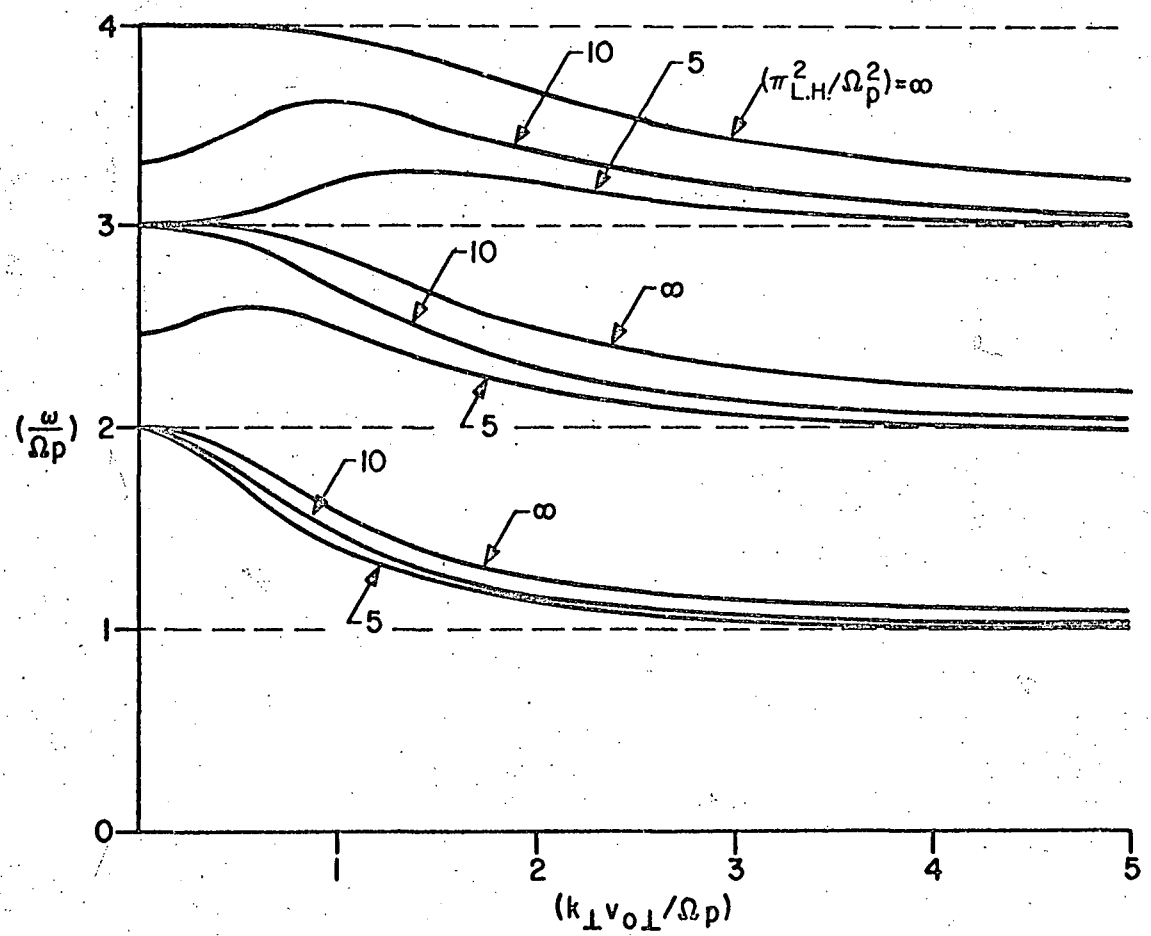

Fig. 15. Dispersion curves or perpendicularly propagating proton CH waves in a Maxwellian plasma. These are based on results of Crawford (1965) and particularized to frequencies less than the electron cyclotron frequency. A sequence of pass bands are defined, the nth mode being confined to frequencies between Ω_p and $(n + 1)\Omega_p$. In the ionosphere $\pi^2_{L.H.}/\Omega^2_p$ will usually be in the range 100 to 300.

Fig. 16a.

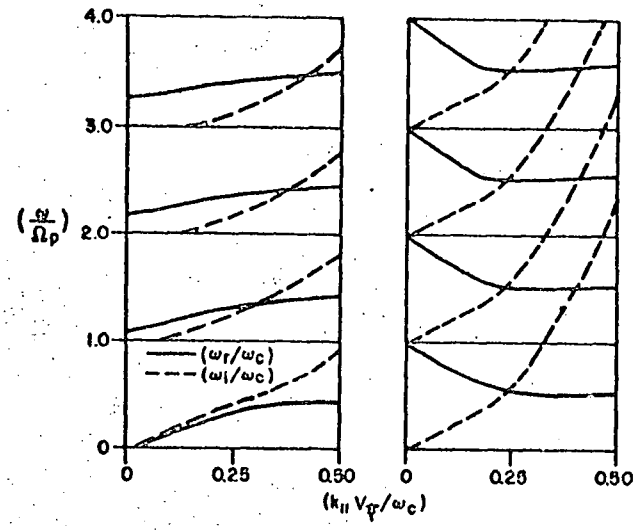

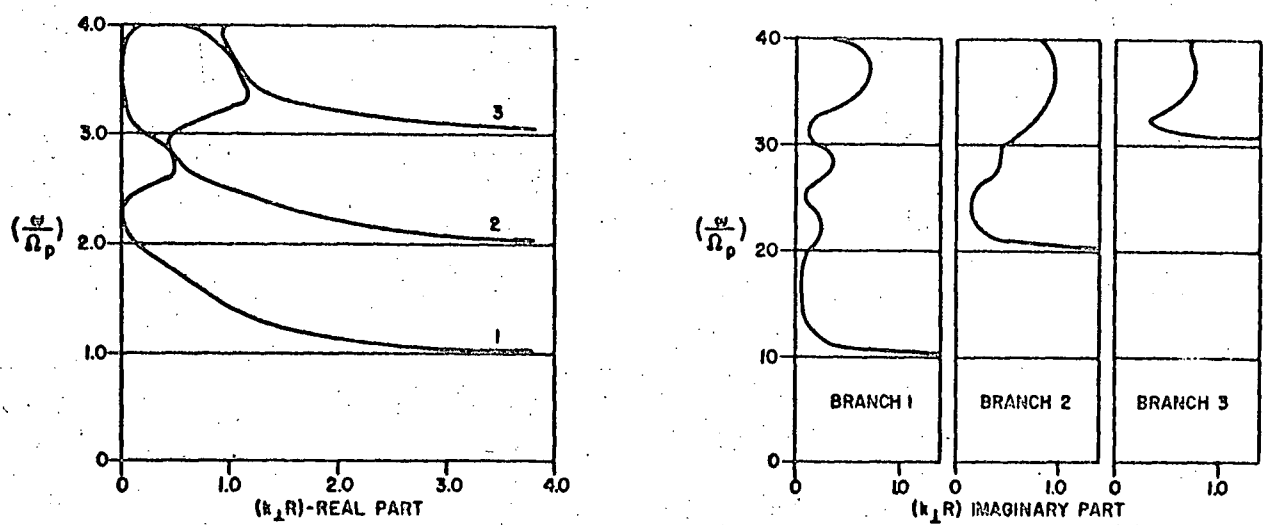

Fig. 16b.

Fig. 16a. Oblique propagation of proton CH waves in a Maxwellian plasma. $\pi^2_{L.H.}/\Omega_p^2 = 20.0$, and $(k_{\perp}\ v_{o\perp}/\Omega_p) = 3.0$. Mode 1 corresponds to the perpendicularly propagating modes, whereas Mode 2 is a new set which exists only for oblique propagation. Curves are based on Crawford (1967).

Fig. 16b. Dispersion curves for perpendicularly propagating proton CH waves in a Maxwellian plasma including collisions. $\pi^2_{L.H.}/\Omega_p^2 = 5.0$ and the collision frequency ν is $\nu/\Omega_p = .05$. These curves are based on results of Tataronis and Crawford (1965).

also to be noted that attenuation for oblique propagation will be, in fact, greater than indicated by Figure 16a, since the electron non-collisional (Landau) damping represented by the term $\{ + i\pi^{\frac{1}{2}}\alpha_{oe}\, e^{-\alpha_{oe}^2}\}$ in Eq. (5.2) has been neglected.

If a small number of collisions are included in the dispersion relation for perpendicularly propagating CH waves in a Maxwellian plasma, then damping as indicated in Figure 16b is obtained. This figure, sketched from Tataronis and Crawford (1965), is for the case of ν/Ω_p (i.e., collisional frequency normalized to the proton gyrofrequency) equal to .05. Ionospheric value of .001 are quite realistic, and thus this damping can be expected to be important. The collisional damping is an inverse function of the group velocity ($d\omega/dk_\perp$), and, as a result, it increases for the higher harmonics.

The perpendicular and oblique propagation of ion CH waves under a variety of non-Maxwellian conditions has been investigated by Hall, Heckrotte and Kammash, (1965). The instabilities found by these authors were classified into two groups: (1) type-A instabilities which occur when propagation is almost exactly perpendicular and the velocity distribution $f_\perp(v_\perp)$ has at least one maxima at other than zero velocity; (2) type-B instabilities which require that the propagation vector have a significant parallel component, but the transverse velocity distribution can decrease monotonically. The relations developed by Hall et al are complicated; no detailed numerical computations of the dispersion is made by these authors. However, it appears that the type-B instabilities are related to the previously mentioned additional modes for oblique propagation of CH waves.

A general requirement derived by Hall et al for type-A instabilities in the first pass band is that

$$< P_1(\beta) > \equiv 2\pi \left(\frac{\Omega_p}{k_\perp}\right)^2 \int_0^\infty d\beta \; J_1^2(\beta) \; f_\perp' \left(\frac{\beta\Omega_p}{k_\perp}\right) > 0$$

where, $J_1(\beta) \equiv$ the Besel function of 1st order,

$$\beta \equiv \frac{k_\perp \; v_\perp}{\Omega_p} ,$$

$f_\perp(v_\perp) \equiv$ the transverse velocity distribution.

Considerations of an elementary physical model for perpendicularly propagating electrostatic waves in a proton gas indicated the physical meaning of $< P_1(\beta) >$ to be a proportionality constant determining the initial direction of energy flow from the particles to the wave.

A necessary condition for instability is clearly $f_\perp'(v_\perp) > 0$ for some $v_\perp$. This, of course, is not true for a Maxwellian distribution. However, $f_\perp(v_\perp)$ is expected to have positive derivative at some velocities in the ionosphere, where a high velocity suprathermal distribution of particles is superimposed on the background Maxwellian distribution. This will be further discussed in the next chapter.

In fact, one of the non-Maxwellian situations discussed by Hall et al consists of such an approximation to the ionosphere. A group of high energy (hot) ions with anisotropic velocity distribution is superimposed on a lower energy (colder) istropically distributed group of the same ion species. The hotter particles can then give up energy to the colder background particles via the mechanism of electrostatic CH waves, The transverse energy of the hot particles is assumed to be much greater than that of the colder particles. As a result, a type-A instability is found. For the idealized situation of a delta function for the transverse distribution

of hot ions, then, at frequencies slightly above the gyrofrequency instability occurs even at very low plasma densities ($\pi_p^2/\Omega_p^2 << 1$), and for small fractions of the total particle density in the hot distribution.

CHAPTER 6

APPLICATION OF THE THEORY OF PROTON CH WAVES TO THE OBSERVATIONS

6.1 Explanation for Specific Observations on the Noise Band

In this section, it will be shown that most of the particular observations on the noise band may be explained as due to proton CH waves propagating in a primarily Maxwellian ionosphere. The sharp, lower frequency cutoffs and harmonic structure are interpreted in terms of waves propagating perpendicularly to the geomagnetic field and both inward and outward with respect to the earth, and the concomitant accessibility conditions. This model is first developed, and then applied to the spectra of Figures 4 to 11.

Waves propagating within the first pass band (i.e., with reference to Figure 15, in the frequency range of one to two times the proton gyrofrequency, Ω_p) will first be considered. Since waves propagate nearly unattenuated in the perpendicular direction, locally observed waves may have been produced and amplified at some distance from the satellite. With reference to Figure 17, consider the satellite at a low or mid-latitude position such as A. All waves propagating upwards to A (i.e., excited in a zone of larger gyrofrequency than at A) may reach A except those produced at frequencies greater than $2\Omega_{pA}$. Waves of frequency $2\Omega_{pA}$ will tend to zero group velocity as they approach the level of A. Similarly, waves propagating downwards and excited above A can propagate to A if they were produced at frequencies greater than Ω_{pA}. Waves at frequency Ω_{pA} will tend to zero group velocity as they approach A. This situation would lead to an observed spectrum of power between Ω_{pA} and $2\Omega_{pA}$ with cutoffs (i.e., decreases in noise intensity) on each side of the band. The sharpness of

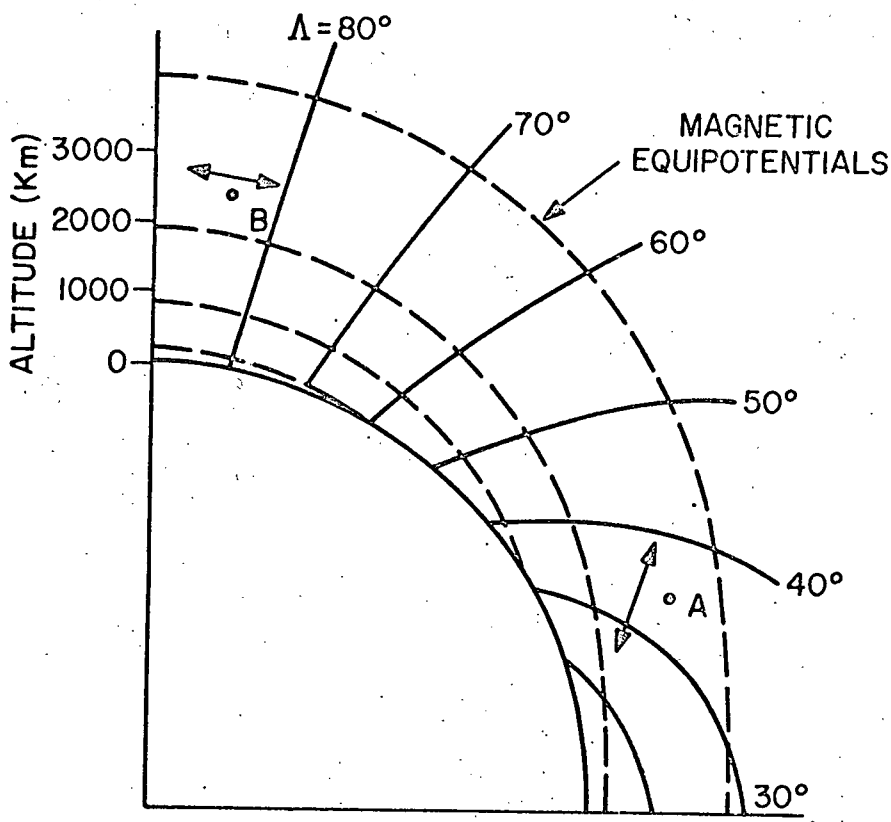

Fig. 17. A cross-section of the earth's magnetic field, reproduced to help visualize the effects of accessibility on proton CH waves.

the cutoffs may be largely controlled by the rate at which collisional damping increases at frequencies near the gyrofrequency harmonics.

The above comments on propagation of CH waves in the first mode may also be applied to waves in the second mode ($2\Omega_p \leq \omega \leq 3\Omega_p$), leading to a band of noise limited by the second and third harmonic of Ω_p. As mentioned in Chapter 5, the higher modes suffer increasingly from collisional damping, and thus may not be observed as frequently as first pass band noise.

At very high latitudes such as point B in Figure 17, accessibility conditions cannot be expected to play such an important part in the shape of the observed spectrum. Waves that propagate perpendicular to the ambient magnetic field will not accumulate at Ω_{pB} and $2\Omega_{pB}$ since they are propagating in a direction of approximately zero gradient in the magnetic field. Under these circumstances, it is expected that the power spectrum obtained at a point such as B will represent the total spectrum of waves produced in the vicinity and not appreciably altered by accessibility conditions. Collisional damping may play a more important part in determining the final shape of the spectrum.

The above discussion of noise band cutoffs is based on the assumption that propagation effects dominate. This is reasonable regardless of the type of instability that excites the waves. For if the instability mechanism is absolute (i.e., temporal growth of the waves at every point to the non-linear limit), then there may be amplification over only a small portion of the frequency range covered by a pass band of the waves; in which case, propagation effects may dominate. The other alternative, convective instability (growth of particular wave fronts as they propagate), is also compatible with the cutoff explanations.

It should also be noted that the cutoffs need not occur exactly at the calculated gyrofrequency, since, as previously mentioned, the dispersion curves of Figure 15 hold strictly only for a Maxwellian plasma, and thus minor deviations could possibly be due to the small non-Maxwellian component of the ionosphere. Upper frequency cutoffs (used in the phenomenological sense) may also be below $2\Omega_p$ for low altitude satellite passes, since, if production and amplification occurs primarily near the gyrofrequency, then the maximum frequency that may be produced will occur near the gyrofrequency at the base of the ionosphere, and this frequency may be less than twice the gyrofrequency at the satellite.

Another factor that may be expected to play an important part in observations of CH waves with a satellite is significant Doppler shifting of the spectrum. From the dispersion relation depicted in Figure 15, the wave phase velocity ($\omega/k_{\perp}$) near the center of the first pass band is of the order of the thermal velocity ($v_{o\perp}$). For a typical ionospheric temperature of 1500° K., $v_{o\perp}$ is 4.3 Km/sec., while the satellite velocity is 6-7 Km/sec. Thus, significant Doppler shifting would be expected for all waves that have wave normals with appreciable components along the satellite velocity vector $\vec{V}$. Since the waves must propagate in the plane perpendicular to the magnetic field, the most pronounced effects are expected to occur when the angle between the velocity vector of the satellite and the geomagnetic field ($\angle(\vec{V},\vec{B})$) is equal to 90°. For a uniform azimuthal distribution of wave normals, only a small percentage of these waves would not be significantly shifted, and thus the noise band would be effectively 'smeared' out.

The spectral features of the noise in Figures 4 to 11 as noted

in Chapter 4 (4.1) will now be interpreted. Each of the predictions from the above model will be considered and the evidence in the Figures for occurrence of the phenomena enumerated:

(1) Lower frequency cutoffs near Ω_p. All the noise bands in the Figures, covering a broad range of latitude and satellite altitudes, have lower frequency cutoffs within 30 Hz of the calculated value. These cutoffs cover the range of about 200 to 650 Hz. This result is expected for CH waves in the lowest pass band.

(2) Harmonic structure. Figure 8 shows a noise band with upper frequency cutoff near $3\Omega_p$. A change in noise level near $2\Omega_p$ is also evident. These observations may be explained as CH waves in the first two pass bands. Figure 9 -- GMT 1918/30-1922/30, and Figure 10 -- GMT 322/00-326/00, indicate more clearly an upper cutoff to the noise band near $2\Omega_p$ and then further noise in the second pass band. These observations are for relatively high satellite altitudes.

(3) Upper frequency cutoff below $2\Omega_p$. The noise bands from satellite passes at altitudes below 1000 Km generally have upper frequency cutoffs below $2\Omega_p$ (Figures 7 and 11). This may be the maximum frequency of waves produced below the satellite.

(4) Doppler shifting. Figure 11, GMT 2024/00-2025/00, exhibits a smearing out of the noise band near the calculated position where $\angle (V,B) \rightarrow 90°$. The situation is complicated by the unexplained noise which comes down from higher frequencies near $\angle (\vec{V},\vec{B}) = 90°$ (seen clearly in Figure 5). Figure 9 -- GMT 1926/30 - 1928/30, and Figure 10 -- GMT 316/00 - 318/00, also show evidence of 'smearing'. This phenomena may be interpreted as due to Doppler shifting.

(5) Shape of spectra changes above $\Lambda = 80°$. Both Figure 9 -- GMT 1913/30 - 1922/30, and Figure 10 -- GMT 324/00 - 326/00, show evidence of a rounding off of the lower frequency cutoff relative to the spectra at lower latitudes. This may be due to the decreased importance of accessibility conditions at these high latitudes.

An additional phenomena of the noise band which may be explained as due to perpendicularly propagating CH waves is "spin modulation". When the antennas are aligned with the magnetic field, the wave electric field and its gradient will be perpendicular to the antenna and thus no signal will be observed. This agrees with the observations. However, there is a definite possibility that the spin modulation is due to the orientation-sensitive gain of the receiver antennas, as discussed in Section 2.2.

An observation, which is not fully explained by the simple model of noise bands due to steady production and amplification of noise, is the structure shown in the Sonograms of Figure 6. Swift (1968) has suggested that similar dispersion (i.e., rising tones) may be due to a convective instability of CH waves propagating from regions of smaller to larger magnetic fields, and is possibly associated with micro-bursts (Parks, (1967); Oliven and Gurnett, (1968)).

Another consideration on this noise band is that it is very difficult to argue conclusively that the observed noise band is in fact an ambient phenomena and not merely excited by the motion of the satellite through the ionospheric plasma. The necessity for considerations of this nature has been discussed by Scarf et al, (1968). The pronounced altitude and latitude dependence of the shape of the spectrum, and also the ~ 50% non-occurrence of the noise band, support the assumption that the waves are ambient.

6.2 Occurrence Pattern of the Noise Band

Without a detailed knowledge of the energy spectrum of the non-thermal particle and the generation mechanism possibly operative for proton CH waves, the occurrence pattern of the noise cannot be fully explained. However, a few remarks may be pertinent.

From Eq. (5.6) it has been noted that a general requirement for type-A instabilities is $< P_1(\beta) > > 0$, and the rate of energy transfer from the particles to the waves is proportional to this quantity. This may account for the pronounced diurnal variation of occurrence, i.e., occurrence increases markedly at dawn and continues high throughout the day. In this connection, a number of remarks have been made by Brice (1964), who discusses a diurnal peak occurrence of chorus between dawn and noon. This diurnal peak is suggested to be due to adiabatic compression of the magnetic field lines by the solar wind and the subsequent increase in the transverse energy of the trapped particles. This process would thus increase $< P_1(\beta) >$ during the day, and the proton CH waves would have the observed diurnal occurrence variation.

Another factor which could contribute to daytime observation of the noise band is the association of daytime LMT with low altitude of the satellite. $< P_1(\beta) >$ is expected to be largest at low altitudes, since this is where the perpendicular energy of the suprathermal particles maximizes. Since the second adiabatic invariant is approximately conserved, then for each charged particle

$$\frac{\frac{1}{2} m v_{\perp}^2}{B} = \text{constant}$$

where $v_{\perp}$ = perpendicular velocity of a particle gyrating around the magnetic field line,

B = the geomagnetic field induction.

Since B maximizes a low altitude, so does $v_{\perp}$.

In regard to the occurrence pattern of sharp lower cutoffs (Figure 13a), it is seen that these are also most probable during the daytime (or, at the associated low altitudes). Considering the model for lower frequency cutoffs due to accessibility conditions on inward propagating waves (Section 6.1), then the occurrence pattern may be due to the possibility of wave production over a wide range of altitudes above the satellite. If the waves can propagate over large distances, the probability of lower frequency cutoffs may be a function of how low the satellite is in the region of wave production. This gives a corresponding maximum occurrence during the daytime (low altitude) passes.

The variation of upper frequency cutoff (Figure 13b) and noise band occurrence with Kp (Figure 14) are somewhat abstruse.

CHAPTER 7

OTHER POSSIBLE EXPLANATIONS FOR THE NOISE BAND

7.1 Results of a Full Wave Treatment of the Bernstein Modes

In Chapter 5, theoretical studies of electrostatic waves, propagating in the vicinity of the proton gyrofrequency, were reviewed. Recently, a full wave (i.e., the electrostatic approximation, $\vec{E} = -\nabla\phi$, is not made) study of waves propagating perpendicular to the ambient magnetic field in a collisionless Maxwellian plasma and at frequencies much less than Ωe, has been completed (Fredricks, (1968a) and (1968b); Fredricks and Scarf, (1968)). These authors termed the resulting wave 'generalized ion Berstein modes'.

Under the condition

$$\left(\frac{k\, v_{o\perp}}{\Omega_p}\right)^2 >> 1, \tag{7.1}$$

it was shown that the electrostatic dispersion results are quite valid if

$$\frac{P_+ \;\; \beta_+ \;\; \omega^2}{(1 + 2\beta_+)\; k^2 \; R_+^2} << 1, \tag{7.2}$$

where

$$R_+ \equiv v_{o\perp}/\Omega_p \; .$$

In the ionosphere at satellite altitudes

$$P_+ \equiv \pi_p^2/\Omega_p^2 \quad \sim \quad 10^3$$

$$\beta_+ \equiv \frac{8\pi\, n_p\, \kappa\, T}{B^2} \quad \sim \quad 10^{-9}$$

For the range of frequencies of current interest, $\omega^2 \sim 10^6\ \mathrm{sec}^{-1}$., and

therefore Eq. (7.2) reduces to

$$\frac{\Omega_p^2}{k_\perp^2 v_{o\perp}^2} << 1.$$

The electrostatic results of Figure 15 will necessarily be accurate if

$$\frac{k_\perp v_{o\perp}}{\Omega_p} \gtrsim 3 .$$

The experimental studies of electron CH waves by Mantie (1967) indicated, under similar conditions of β and P for electrons, an excellent agreement between experiment and electrostatic theory for $k\, v_{o\perp}/\Omega_p$ as small as 0.1.

For a low β_+, collisionless Maxwellian plasma of protons and electrons, Fredricks and Scarf (1968) suggested the qualitative dispersion curves shown in Figure 18. It is seen that for any particular mode, there are three regions of $k_\perp$ where the group velocity $\frac{d\omega}{dk}$ approaches zero. The explanation for noise bands with upper and lower frequency cutoffs, as outlined in Chapter 6, is based on the zeros of the groups velocity for finite values of $k_\perp$ (i.e., on the electrostatic portion of the curves). However, the possibility of noise bands with lower and upper frequency cutoffs could also be supported by the primarily electromagnetic portions of the curves. Again there is a range of $k_\perp$ bounded by zeros in the group velocity. The same conditions on accessibility conditions may be applied as for the electrostatic waves.

A number of difficulties are associated with such an electromagnetic origin to the observed noise bands. Possibly, collisions will lead to interaction between waves in the different electromagnetic modes causing the cold plasma treatment to be a good approximation to the dispersion. Further study is needed in order to estimate the

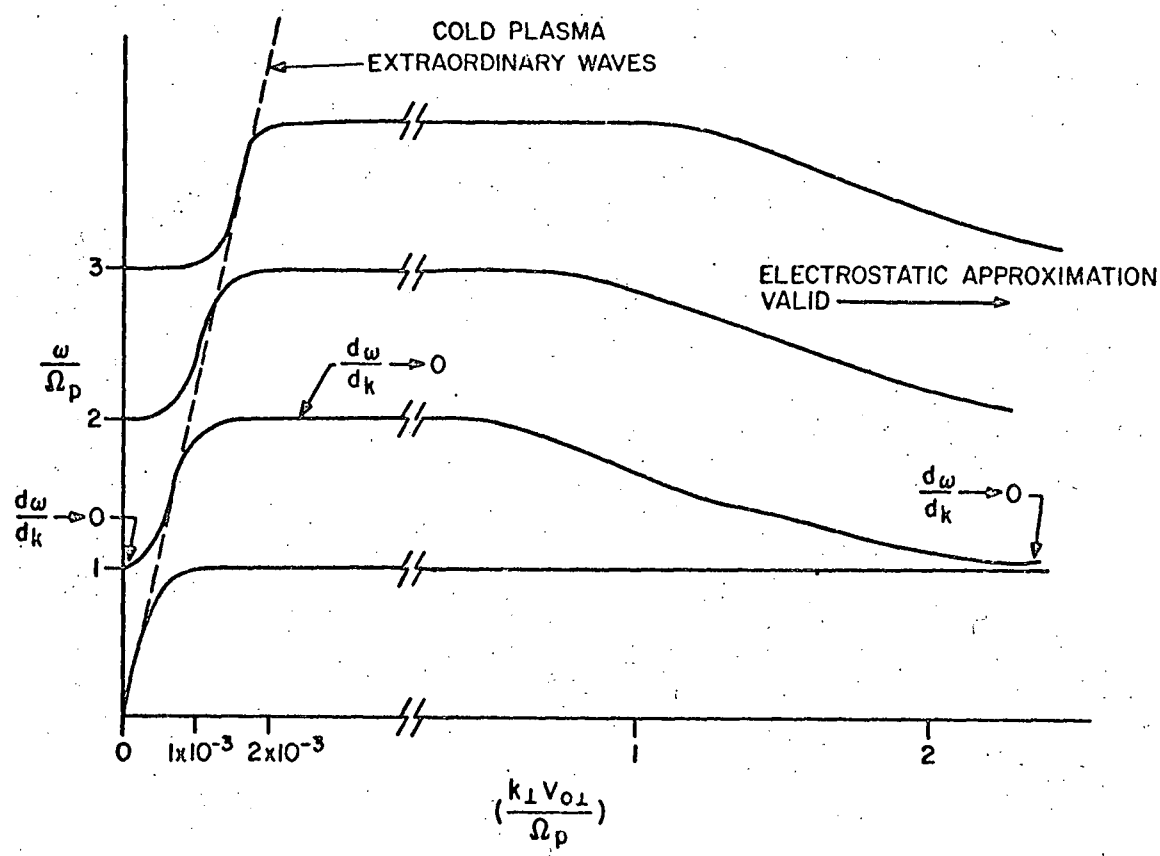

Fig. 18. Schematic of 'generalized ion Bernstein mode' dispersion. These curves are based on the results of Fredricks and Scarf (1968), and are for a low $\beta+$ plasma. Note the change in scale on the horizontal axis.

collisional effects. In addition, a basic problem with an electromagnetic origin of the noise is the observation of dependence of the spectral shapes on $\angle(\vec{V},\vec{B})$. Phase velocities for electromagnetic waves in the ionosphere are ~ 10^4 km/sec; this is much larger than the satellite velocity, and thus such waves cannot be significantly Doppler shifted. Thus, it appears that at least some of the waves observed must be electrostatic.

7.2 L=0 Theory

Noise bands of a nature very similar to those investigated in this paper have been reported by Burns (1966) and Gurnett and Burns (1968) from Injun III data. These authors reported a lower frequency cutoff which usually occurs below the proton gyrofrequency, and noted particularly the systematic decrease of this frequency with increasing altitude.

Gurnett and Burns proposed an explanation for such a noise band based on propagation effects on right-hand polarized (whistler) electromagnetic waves. The existence of whistler mode waves of appropriate frequency and propagating down magnetic field lines from high altitudes, was postulated. The effects of increasing proton gyrofrequency and decreasing relative abundance of hydrogen seen by the downcoming wave may be understood in terms of the theory outlined by Gurnett et al (1965); these authors considered propagation of ELF electromagnetic waves in a plasma of electrons, H^+, He^+, and O^+. Whistler mode (right-hand polarized) waves propagating parallel to the geomagnetic field and at frequencies slightly less than the local proton gyrofrequency can 'cross-over' to the left-hand polarized mode. These waves are reflected at a lower altitude corresponding to the cutoff frequency of left-hand waves

(L=0 frequency, in the notation of Stix, (1962)). As it turns out, L=0 frequency is a decreasing function of altitude. Thus, higher frequency energy is reflected at lower altitudes and vice versa. These conditions lead to a noise band with a lower frequency cutoff at the local L=0 frequency near the satellite. Noise seen at the cutoff is due to waves being reflected at the L=0 frequency near the satellite. Noise seen in the band at higher frequencies would be due to waves which propagate to altitudes below the satellite and then are reflected.

However, the L=0 frequency varies almost linearly in the frequency range $\frac{\Omega_p}{4}$ ($\Omega_p \equiv$ proton gyrofrequency) to Ω_p for relative abundances of hydrogen ion from ~ 1.0 to ~ 0.0, respectively. This variation is fairly independent of the relative abundance of O+. Gurnett and Burns explain observed noise band cutoffs which occur near Ω_p in the protonosphere (where relative abundance of H is ~ 1 and consequently the L=0 frequency is near $\Omega_p/4$) as possibly due to waves propagating downwards initially at an appreciable angle to the magnetic field, and thus being reflected before reaching the L=0 level for each frequency component. A sharp cutoff of such a noise band would require considerable order in the initial (non-zero) wave normal angles.

On the basis of the above theory it is thus difficult to interpret the observations presented in this thesis. Besides the problem of order in the wave-normal angle distribution, apparent Doppler shifting and the upper frequency cutoff of the noise band are not accounted for.

CHAPTER 8

SUMMARY AND CONCLUSIONS

ELF noise bands in the ionosphere which have a lower frequency cutoff near the local gyrofrequency have been investigated. Data from the Alouette II satellite was spectrum analyzed, using both existing analog methods and a digital spectral analysis program.

The digital spectral analysis of the noise band indicated that, at all satellite altitudes and latitudes, the sharp lower frequency cutoffs conform to the calculated proton gyrofrequency to within ~ 30 Hz. This result is taken as strong support for the hypothesis that the noise band was due to proton CH waves. In addition, this hypothesis is supported by the consistent manner in which the following aspects of the noise band may be interpreted:

(1) the sharp upper and lower cutoffs of the noise band, as due to accessibility conditions and accumulation of waves where the group velocity goes to zero,

(2) the change from sharp to diffuse lower cutoff of the noise band when the satellite travels to very high latitudes, as due to changing accessibility conditions,

(3) smearing out of the spectrum at satellite positions where $\angle(\vec{V},\vec{B}) \sim 90$, as due to Doppler shifting of a large portion of the wave spectrum,

(4) the upper frequency cutoff of the band below $2\Omega_p$ which occurs at low latitudes and altitudes, as due to the region of production of the waves being primarily at higher altitudes.

The occurrence patterns of the noise band were derived from 971 observations on the noise band spaced at 4-5 minute intervals, using

available Rayspan data for epoch 1966. The diurnal variation with maximum occurrence on the dayside of the earth was interpreted in terms of the regions where transverse energy of suprathermal particles maximizes, and therefore probability of excitation of perpendicularly propagating CH waves is greatest.

The cyclotron harmonic wave hypothesis thus provides a consistent explanation for a large portion of the observations on the noise band.

Future work is indicated, particularly in regard to studying CH wave instabilities using realistic models of the suprathermal velocity distributions. It would also be useful to investigate the effects of collisions on the full wave treatment of Bernstein modes in order to adjudge the importance of gyrofrequency effects indicated by Fredricks (1968). The work presented in this thesis also directs attention to the continuing need in satellite VLF experiments of both a magnetic loop antenna and electric antenna on the same vehicle, in order to sort out electromagnetic and electrostatic waves in the ionospheric plasma.

APPENDIX

SPECTRAL ANALYSIS FROM THE DIGITIZED RECORDS

The power spectrum estimation was carried out using methods obtained from Blackman and Tukey (1959) and Bingham, Godfrey, and Tukey (1967). This section will aim at tying together some of the ideas in these references, and at outlining the practical analysis as performed.

It is known from continuous record analysis that

$$P(f) = \lim_{T \to \infty} \frac{1}{T} \left| \int_{-T/2}^{+T/2} X(t) \cdot \ell^{-i2\pi ft} \, dt \right|^2 \tag{A.1}$$

where $P(f)$ = the power spectrum of the stationary random process,

f = frequency

T = length of the record.

Define the functions $D_i(t)$ subject to the restrictions that it be piecewise continuous and

$$D_i \ (t \leq 0) = D_i \ (t \geq T_n) = 0 \ , \quad D_i \left(\frac{T_n}{2}\right) = 1 \ ,$$

for some value of T_n representing the length of record to be analyzed. Such functions will be called "data windows" on account of the following definition. Let

$$X_i(t) \equiv D_i(t) \cdot X(t) \tag{A.2}$$

Also, define

$$P_i(f) \equiv \frac{1}{T_n} \left| \int_o^{T_n} D_i(t) \cdot X(t) \cdot \ell^{-2\pi ift} \, dt \right|^2 \tag{A.3}$$

$$G(t) \equiv \begin{cases} \dfrac{X(t)}{T_n^{\frac{1}{2}}} \ , & 0 \leq t \leq T_n \\ 0 \ , & t \leq 0 \ \text{ or } \ t \geq T_n \end{cases} \tag{A.4}$$

The Fourier transforms of D_i and G are then

$$Q_i(f) = \int_{-\infty}^{+\infty} D_i(t)\, \ell^{-i2\pi ft}\, dt \quad , \tag{A.5}$$

and

$$S_a(f) + \frac{1}{T_n^{\frac{1}{2}}} \int_{-\infty}^{+\infty} G(t)\, \ell^{-i2\pi ft}\, dt \ , \tag{A.6}$$

where the subscript 'a' stands for apparent. Considering ergodicity, the ensemble average of $S_a(f)$ (over an infinite set of processes identical to that which produced X(t)) is

$$\text{avg} \cdot \left\{ S_a(f) \right\} = \left| S(f) \right|^{\frac{1}{2}} = P(f) \tag{A.7}$$

where

$$S(f) = \underset{T_n \to \infty}{\text{limit}} \frac{1}{T_n^{\frac{1}{2}}} \int_{-Tn/2}^{+Tn/2} X(t)\, \ell^{-i2\pi ft}\, dt \ . \tag{A.8}$$

Using the convolution theorem with Eqs. (A.3), (A.5), and (A.6);

$$P_i(f_1) = \frac{1}{T_n} \left| \int_{-\infty}^{+\infty} Q_i(f_1 - f) \cdot S_a(f)\, df \right|^2 \tag{A.9}$$

for every frequency f_1. This relation exhibits $P_i(f_1)$ as the result of looking at a Fourier transform of the truncated process X(t) through a filter (called a 'spectral window') $Q_i(f_1-f)$ of variable transmission properties. In most cases it is desired to look at $S_a(f)$ over a narrow band of frequencies surrounding f_1.

Two particular data windows are

$$D_o'(t) = \begin{cases} 1 \ , & |\, t \,| < T_{n/2} \\ \frac{1}{2} \ , & |\, t \,| = T_{n/2} \\ 0 \ , & |\, t \,| > T_n \end{cases} \tag{A.10}$$

and

$$D_2'(t) = \frac{1}{2}\left(1 + \cos\frac{2\pi t}{T_n}\right)^{\dagger} \tag{A.11}$$

Their Fourier transforms are:

$$A_0'(f) = T_n \frac{\sin \pi f T_n}{\pi f T_n} \tag{A.12}$$

and,

$$Q_2'(f) = \frac{1}{2} Q_0'(f) + \frac{1}{4}\left[Q_0'(f + \frac{1}{T_n}) + Q_0'(f - \frac{1}{T_n})\right]^{\dagger\dagger}$$

Use of either D_2' or the alternative Q_2' is called 'hanning'. The transform pairs are shown in Figure 19.

It is recognized that applying a data window of the type $D_o(t)$ is equivalent to taking a signal of finite length T_n. Reference to the figure shows that this 'chopping-off' of the signal corresponds to a spectral window which has relatively large side lobes. Thus, any particular spectral estimate will be considerably influenced by the rest of the spectrum. This situation can be improved by applying a hanning window. This is done by multiplying $D_2(t)$ into the signal or by transforming the unmodified data $D_0(t) \cdot X(t)$ and convolving $S_a(f)$ with $Q_2(f)$ using the 'shifted' Eq. (A.13). From the figure, it is seen that $Q_2(f)$ will lead to spectral estimates integrated over a larger interval around a particular frequency than would result from $Q_o(f)$. However, side lobe effects are reduced sufficiently for present purposes.

It is convenient that the concepts and equations of spectrum

---

†So subscripted to conform with Blackman and Tukey (1959).

††The D_i' and Q_i' may be converted to the corresponding unprimed functions using the relations:

$$D_i'(t) = D_i(t + T_{n/2}),$$
$$Q_i'(f) = \ell^{i\pi f T_n} \cdot Q_i(f).$$

This gives,

$$Q_2(f) = \frac{1}{2} Q_o(f) - \frac{1}{4}\left[Q_o(f + \frac{1}{T_n}) + Q_o(f - \frac{1}{T_n})\right]$$

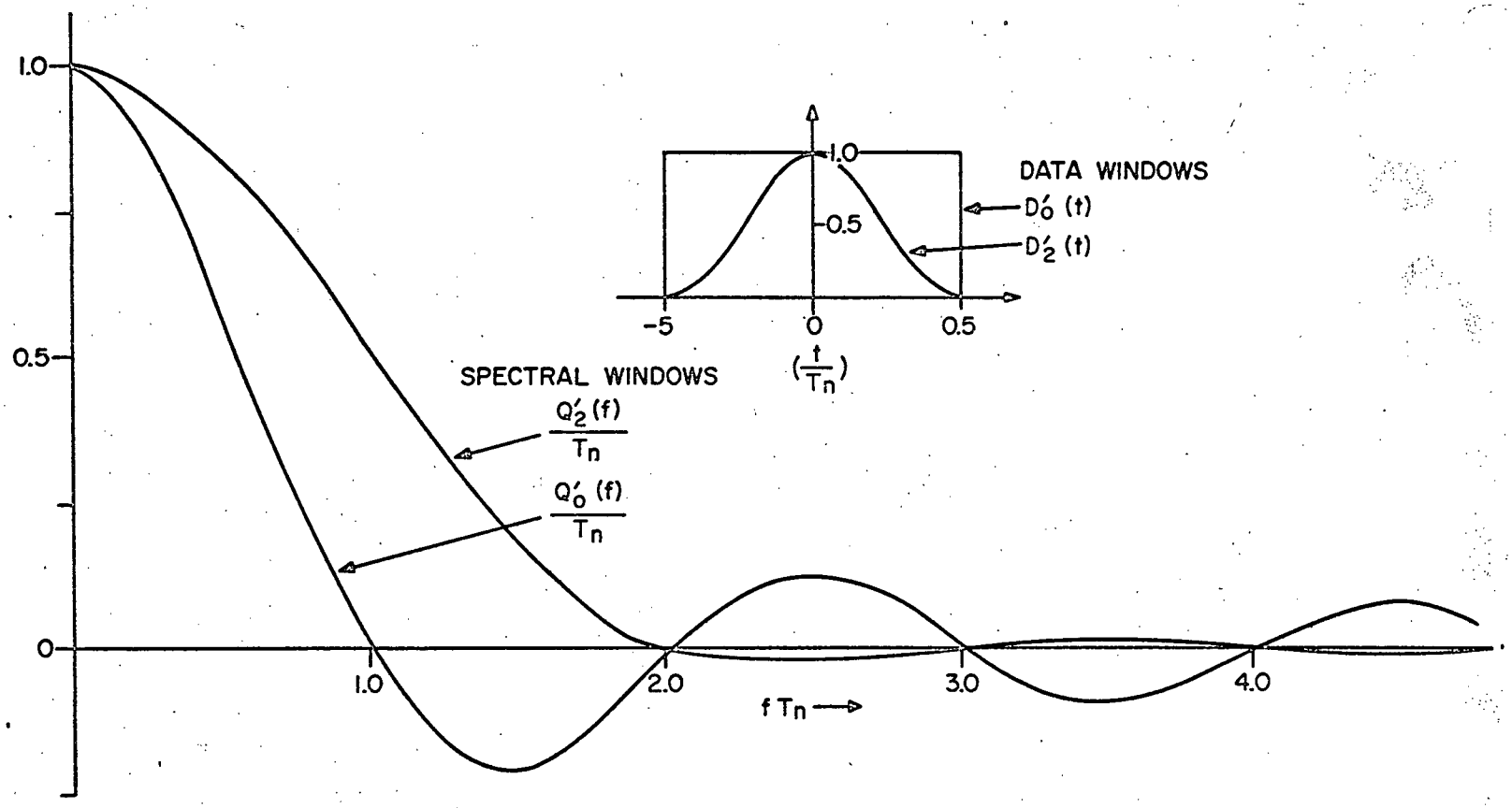

Fig. 19. Data windows and corresponding spectral windows, adapted from Blackman and Tukey (1959).

analysis on continuous records may be converted directly into forms appropriate for digital spectral analysis of discrete time series. The finite discrete time series corresponding to a signal X(t) is obtained by sampling X(t) at intervals Δt for a time T_n, the length of record to be studied. The time series will be denoted by

$$X_0 , X_1 , X_2 , \ldots, X_{N-1}$$

where

$$N = \frac{T_n}{\Delta t} = \text{the number of samples taken.}$$

A power density spectrum is then defined as

$$P_r \equiv \frac{1}{T_n} \left| \sum_{k=0}^{N-1} X_k \, \ell^{-2\pi i k \left(\frac{r}{N}\right)} \right|^2 , \quad r = 0, 1, \ldots, N-1 \qquad (A.14)$$

in analogy with Eq. (A.13), and where frequency is normalized to $1/N \cdot \Delta t$. The expression within the absolute value signs is called the digital Fourier transform, and may be quickly computed using the 'fast Fourier transform' algorithm.

If f_r denotes the Fourier coefficients from the digital Fourier transform, that is

$$f_r \equiv a_r + ib_r = \sum_{k=0}^{N-1} X_k \, \ell^{-2\pi i k \left(\frac{r}{N}\right)} , \quad r = 0, 1, \ldots, N-1, \qquad (A.15)$$

then for N even, and real X_k's, it can be shown that

(a) f_o is real

(b) $fN/2$ is real

(c) $f_{\frac{N}{2}+\ell} = f^*_{\frac{N}{2}-\ell}$ for $\ell = 1, 2, \ldots, \frac{N}{2} - 1$. (A.16)

Thus, the coefficients need only be calculated for $r = 0, 1, 2, \ldots, \frac{N}{2}$. These cover the frequency range from 0 to $f_N = \frac{1}{2\Delta t}$. f_N is called the

'Nyquist' or 'folding' frequency, and will be discussed further.

A hanning window may be applied, as previously indicated, on the X_k or the Fourier coefficients of the transformed data. That is, for hanning in the frequency domain, the following operation is performed:

$$\left.\begin{aligned} A_r &= -\frac{1}{4}a_{r-1} + \frac{1}{2}a_r - 1/4\, a_{r+1} \\ B_r &= -\frac{1}{4}b_{r-1} + \frac{1}{2}b_r - 1/4\, b_{r+1} \end{aligned}\right\} \quad r = 1, \ldots, \frac{N}{2} - 1$$

$$A_o = \frac{1}{2}(a_0 - a_1) \tag{A.17}$$

$$A_{\frac{N}{2}} = \frac{1}{2}\left(a_{\frac{N}{2}} - a_{\frac{N}{2}-1}\right)$$

$$B_o = B_{\frac{N}{2}} = 0$$

where the last three expressions are derived with the help of (A.16). A_r and B_r are then the hanned Fourier coefficients. The modified power spectrum estimates are

$$P'_r = \frac{1}{T_n}(A_r^{\,2} + B_r^{\,2}) \tag{A.18}$$

An additional problem in digital Fourier analysis which doesn't appear in the continuous analysis is 'aliasing'. This concept is explained in detail by Blackman and Tukey (1959). In a digital power spectrum analysis, power at frequencies above f_N will be folded back into the estimates for power below f_N. The manner in which this happens is illustrated in the following schematic:

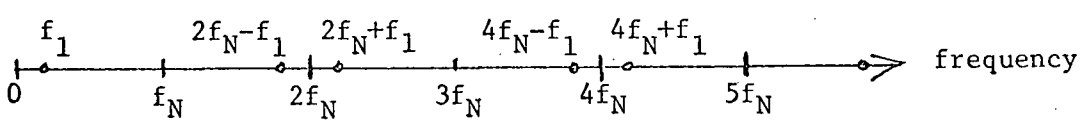

Power is distributed in frequency above and below f_N before folding.

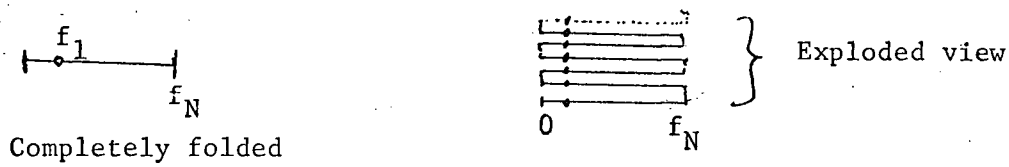

All power at frequencies $f_N \pm f_1$, n = 0, 2, 4, ..., will appear in our estimate of power at f_1 in the frequency interval $[0, f_N]$.

The practical way to avoid this problem is to use an analog filter which passes only those frequencies below f_N. The desired Nyquist frequency is chosen by the sampling rate. In the case at hand it was desired to study the real-time frequency range of 0-1000 Hz. In order to save computer time, the playback tape speed of the signal was twice the real-time record rate. The signal out of the tape recorder was fed through a filter, set to have an upper pass limit of 2 KHz. Attenuation above this frequency was 20 dB per octave. The sampling frequency, chosen to be 8 K $\frac{\text{samples}}{\text{sec}}$, gave Nyquist frequency of 4 KHz. Thus, for a reasonably flat spectrum, any noise folded back into the frequency range of prime interest (0-2000 Hz for twice real-time playback tape speed), would come from frequencies $\gtrsim$ 5 KHz. This folded back noise would thus be $\gtrsim$ 30 dB down.

Another important consideration in spectral analysis is some estimation of the statistical stability of the spectral estimates. This stability can be understood in terms of the chi-square distribution.

"If $y_1, y_2, \ldots, y_k$ are independently distributed according to a standard normal distribution, that is, according to a Gaussian distribution with average zero and unit variance (and, consequently, unit standard deviation), then

$$\chi_k^2 = y_1^2 + y_2^2 + \ldots + y_k^2 \quad ,$$

which is obviously positive, follows, by definition of a chi-square distribution with k degrees of freedom. The coefficient of variation of χ_k^2 , the ratio of RMS deviation to average value is $(2/k)^{\frac{1}{2}}$, so that as k increases, χ_k^2 becomes relatively less variable. This statement also applies to any multiple of χ_k^2." †

From equation (A.18),

$$P_r' = \frac{1}{T_n} (A_r^2 + B_r^2)$$

where A_r and B_r are the real and imaginary part of the hanned Fourier coefficient for the rth power spectrum estimate. If the noise is random (phase and amplitude at any frequencies are not stably related), then the A_r and B_r will be independently distributed. Use of the hanning window leads to spectral estimates which do not greatly overlap in the frequency domain; each spectral estimate should follow a chi-square distribution with k=2 degrees of freedom.

To increase the stability of the estimates (increase k), if the noise source is stationary, then individual analyses on m successive records of length T_n may be made and the results combined. The estimate at each frequency is taken to be the arithmetic mean of the corresponding estimates in each of the analyses. As a result, each spectral estimate (which is effectively averaged over a time period of $m \cdot T_n$ and a bandwidth of $\frac{1}{T_n}$) now has $k=2 \cdot m$ degrees of freedom.

Degrees of freedom may also be gained by taking the arithmetic mean of neighbouring spectral estimates and using them as single estimates of power at mean frequencies;

$$\text{i.e.,} \quad P_r' = \frac{P_{2r-1} + P_{2r}}{2} \qquad r = 1, 2, \ldots, N/4$$

The estimates P_r' will have twice as many degrees of freedom as the P_r.

---

† Blackman and Tukey (1959)

BIBLIOGRAPHY

Barrington, R.E. and R.W. Harvey. Alouette II Observations of VLF Electric Field Amplitudes. To be presented at Spring URSI, Washington, D.C. (1969).

Bernstein, I.B. Waves in a Plasma in a Magnetic Field. *Phys. Rev.* 109, 10-21 (1958).

Bingham, C., M.D. Godfrey and J.W. Tukey. Modern Techniques of Power Spectrum Estimation. *IEEE Trans. Audio and Electro-acoustics*, AV-15, 56 (1967).

Blackman, R.B. and J.W. Tukey. *The Measurement of Power Spectra*, Dover, New York (1959).

Brice, N. A Qualitative Explanation of the Diurnal Variation of Chorus. *J. Geophys. Res.*, 69, 4701 (1964).

Burns, T.B. A Study of VLF Noise Bands with the Injun 3 Satellite. Paper presented at the Fall URSI Meeting, Palo Alto, Calif. (1966).

Cain, J.C., S.J. Hendricks, R.A. Langel and W.V. Hudson. A Proposed Model for the Internation Geomagnetic Reference Field, 1965. *J. Geomag. Geoelect.*, 19, 335 (1967).

Crawford, F.W. A Review of Cyclotron Harmonic Phenomena in Plasmas. *J. Nucl. Fusian*, 5, 73 1965.

Dickinson, P.G.H. Positive Ion Sheaths Due to $\vec{V}x\vec{B}$. I.M. 123. Department of Scientific and Industrial Research, Radio Research Station, U.K. (1964).

Fredricks, R.W. Structure of the Bernstein Modes for Large Values of the Plasma Parameter. *J. Plasma Phys.*, 2, 197 (1968a).

Fredricks, R.W. Structure of Generalized Low Frequency Bernstein Modes from the Full Electromagnetic Dispersion Relation. *J. Plasma Phys.*, 2, 365 (1968b).

Fredricks, R.W., and F.L. Scarf. Electromagnetic and Electrostatic Bernstein Modes in a Warm Collisionless Maxwellian Plasma. Presented at NATO Advanced Study Institute, "Plasma Waves in Space and in the Laboratory", Röros, Norway, (1968).

Gurnett, D.A., S.D. Shawhan, N.M. Brice and R.L. Smith. Ion Cyclotron Whistlers. *J. Geophys. Res.*, 70, 1665 (1965).

Gurnett, D.A. and T.B. Burns. The Low Frequency Cutoff of ELF Emissions. *J. Geophys. Res.*, 73, 7437 (1968).

Gurhart, H., T.L. Crystal, B.P. Ficklin, W.E. Blair and T.J. Yung. Proton Gyrofrequency Band Emissions Observed Aboard OGO 2. *J. Geophys. Res.*, 73, 3592 (1968).

Hall, L.S., W. Heckrotte, and T. Kammash. Ion Cyclotron Electrostatic Instabilities. *Phys. Res.*, 139, A1117 (1965).

Harp, R.S., The Dispersion Characteristics of Longitudinal Plasma Oscillations near Cyclotron Harmonics. *Proc. 7th Internat. Conf. on Phenomena in Ionized Gases.* Belgrade (1965).

Henderson, D.P. and O.L. Cote. Technical Details and Electrical Evaluation of the VLF Receivers Mk I and Mk II for S27A. TM No. 482. Defence Research Telecommunications Establishment, Ottawa, Ontario, (1964).

*

Hoffman, J.H. Ion Mass Spectrometer on Explorer XXXI Satellite. IEEE Special Issue on ISIS Program. In Press (1969).

Mantie, T.D. Cyclotron Harmonic Wave Phenomena. SUIPR Report No. 194, Institute of Plasma Res., Stanford U., Stanford, Calif. (1967).

O'Brien, B.J., C.D. Laughlin, J.A. Van Allen, and L.A. Frank. Measurements of the Intensity and Spectrum of Electrons at 1000 - kilometer Altitude and High Latitudes. *J. Geophys. Res.*, 67, 1209 (1962).

Oliven, M.N. and D.A. Gurnett. Microburst Phenomena. 3. An Association between Microbursts and VLF Chorus. *J. Geophys. Res.*, 73, 2355 (1968).

Parks, G.K. Spatial Characteristics of Auroral-Zone X-Ray Microbursts. *J. Geophys. Res.*, 72, 215 (1967).

Scarf, F.W., R.W. Fredricks and G.M. Crook. Detection of Electromagnetic and Electrostatic Waves on OV3-3. *J. Geophys. Res.*, 73, 1723 (1968).

Stix, T.H. *The Theory of Plasma Waves.* McGraw-Hill, New York (1962).

Storey, L.R.O. The Design of an Electric Dipole Antenna for VLF Reception within the Ionosphere. Tech. Rept. 308 TC, *Centre National d'Etudes des Télécommunications*, Dept. 'Télécommande', Paris (1963).

Swift, Daniel W. A new Interpretation of VLF Chorus. *J. Geophys. Res.*, 73, 7447 (1968).

Tataronis, J.A. Cyclotron Harmonic Wave Propagation and Instabilities. SUIPR Report No. 205, Institute for Plasma Research, Stanford U., Stanford, California (1967).

*

Hendricks, S.J. and Cain, J.C. Magnetic Field Data for Trapped-Particle Evaluations. J. Geophys. Res., 71, 346(1966).

Tataronis, J.A. and F.W. Crawford. Cyclotron and Collision Damping of Propagating Waves in a Magnetoplasma. *Proc. 7th Internat. Conf. on Phenomena in Ionized Gases*, Belgrade (1965).

Taylor, William W.L. and Donald A. Gurnett. Morphology of VLF Emissions Observed with the Injun 3 Satellite. *J. Geophys. Res.*, 73, 5615 (1968).